Thermal Activation of PEDOT:PSS/PM6:Y7 Based Films Leads to Unprecedent High Short-Circuit Current Density in Nonfullerene Organic Photovoltaics

Enas Moustafa, Maria Méndez, José G. Sánchez, Josep Pallarès, Emilio Palomares,* and Lluis F. Marsal**

Finding an effective approach to suppress trap formation is a potential route for enhancing the performance of nonfullerene organic photovoltaic (NF-OPVs) devices. Here, an extraordinary short-circuit current density (J_{SC}) value of 32.65 mA cm^{-2} is achieved, higher than the state-of-the art NF-OPVs reported, reaching a high power conversion efficiency (PCE) of 17.92%. This remarkable enhancement is exhibited through the fine-tuning of PEDOT:PSS/PM6:Y7 films and interface morphologies via applying the prethermal treatment approach (Pre-TT) to the devices, which exhibit J_{SC} and PCE enhancement of 21% and 8%, respectively, compared to the pristine devices. Accordingly, the dependence of the J_{SC} upon the Pre-TT approach through a range of morphological, optical, electrical, and advanced transient measurements is investigated. The Pre-TT-based films are found to possess optimal smooth blend morphology with better dispersity owing to reduced domain size. Moreover, the measurements show that the optimized treated devices present higher exciton dissociation probabilities and generation rate of the free charge carriers, showing an ideal balanced electron/hole mobility that reveals the J_{SC} and PCE enhancement. Hence, Pre-TT approach provides a facile passivation strategy that reduces the trap state density of the blend film, improves interface charge transfer, allows balanced electron/hole mobility, and thus promotes device performance.

1. Introduction

Over the past two decades, tremendous efforts have been dedicated to organic photovoltaics (OPVs) which have led to the breaking barrier of 20% power conversion efficiencies (PCEs) for single-junction devices.[1–7] Recently, the non-fullerene low bandgap acceptor materials (NFA) receive considerable attention regarding their thermal stability,[8,9] broad absorption spectrum which lead to efficient solar photons harvesting and thus high output current density,[10] diminishing the nonradiative energy losses, providing high voltages,[11,12] and easy tunable energy level.[5,13,14] From the device point of view, enhancing both photocurrent and photovoltage of NF-OPVs are the most straightforward strategy to improve the photovoltaic performance.[1] In addition, it is well known that the molecular orientation between the donor and acceptor materials plays a vital role in the charge transfer kinetics.[15] Hence, the anisotropic structure of NFA (such as Y6 and Y7) secures an efficient π–π interaction that matches the coupling with the donors which tuned the phase separation.[16] As a result, the NF-OPVs demonstrate an efficient capability by separating excitons with negligible driving energies, obtaining high PCEs with respect to the energy levels of the used donor materials.[17,18] Thus, these remarkable advantages, avoiding the trade-off behavior between the voltage loss and charge generation,[19] provide barrierless free charge generation, suppressed charge carrier recombination, and enhanced charge mobilities of the resulting devices.[5,19,20]

Furthermore, the device structure as well as the bulk morphology and thickness play a crucial role that critically influences the performance of the NF-OPVs.[19,21,22] These factors mainly control the exciton binding energy and diffusion length[23] to avoid the undesirable static disorder that exhibits intrinsic sources of traps in the devices and in turn affecting the overall performance.[24,25] Upon these contexts, several optimization strategies were performed to control the phase morphology and thicknesses of the photoactive layer of the NF-OPVs.[23,26–29] Furthermore, thermal treatment is one of the effective avenues conducted to tune the bulk and interface

E. Moustafa, J. Pallarès, L. F. Marsal
Department of Electric
Electronic and Automatic Engineering
Universitat Rovira i Virgili
Avda. Països Catalans 26, Tarragona 43007, Spain
E-mail: josep.pallares@urv.cat; lluis.marsal@urv.cat

M. Méndez, J. G. Sánchez, E. Palomares
Institute of Chemical Research of Catalonia (ICIQ-BIST)
Av. Països Catalans 16, Tarragona 43007, Spain
E-mail: epalomares@iciq.es

E. Palomares
ICREA
Passeig Lluís Companys, 23, Barcelona E-08010, Spain

The ORCID identification number(s) for the author(s) of this article can be found under https://doi.org/10.1002/aenm.202203241.

DOI: 10.1002/aenm.202203241

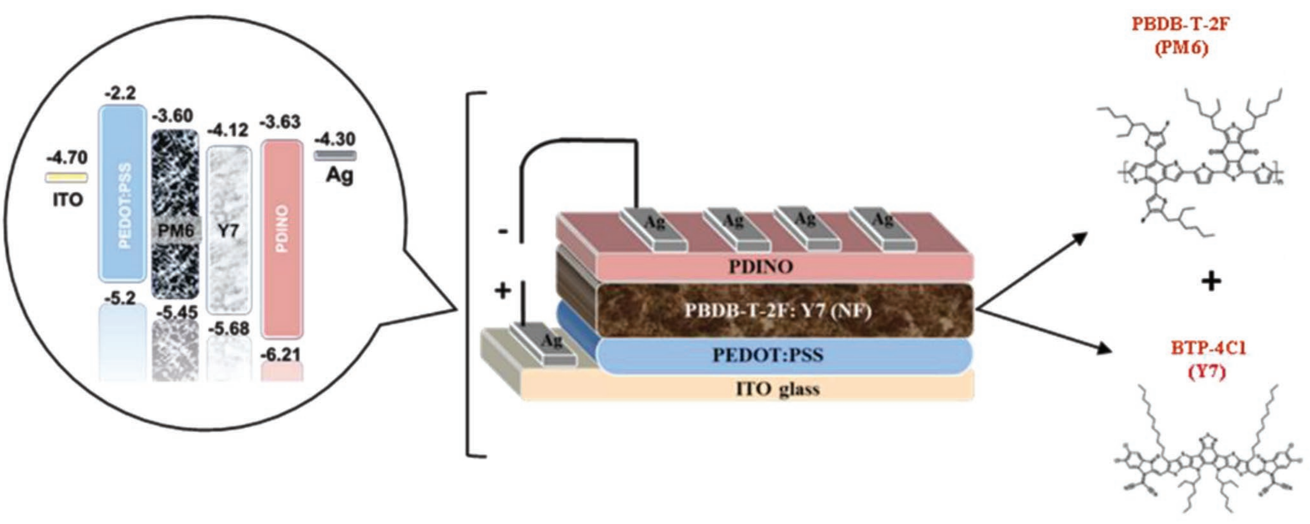

Figure 1. The schematic diagram of the fabricated conventional NF-OPVs structure with the energy band cascade and PM6:Y7 chemical structures. The energy positions of the band edges for the semiconductors and the metals work functions were taken from refs. [4,37,38].

morphologies to perform an efficient charge separation at the donor/acceptor interface[30,31] as well as to modify the interfaces between the active blend and the interfacial layers to enhance the charge carrier collection and transportation.[13,32–35] For instance, the morphology defects described by Wu et al. were the main obstacles that hinder the hole transfer from Y6 to PM6, limiting the exciton decay and consequently declining the overall cell performance.[36] These observations reflect the improvement ability of the NF-OPVs through fine tuning of the active blend and interfacial morphologies.

Accordingly, in the present work, we report pioneer remarkable enhancement in the generated current density (J_{SC}) of 32.62 mA cm^{-2} with a maximum PCE of 17.92% for the optimized single junction NF-OPVs by introducing pre-thermal treatment approach (Pre-TT). The proposed device architecture is ITO/PEDOT:PSS/PM6:Y7/PDINO/Ag as shown in **Figure 1**, the fabricated NF-OPVs based on the active layer blend of PM6 as a polymer donor and the chlorinated Y7 as an acceptor. The interfacial layers are the PEDOT:PSS as a hole transporting layer and PDINO as an electron transporting layer. We presented an interesting dependence of the blend and interface morphologies along with the J_{SC} and in turn the overall device photovoltaic performance upon the applied Pre-TT to the PEDOT:PSS/PM6:Y7 layers.

The Pre-TT approach procedure was described in detail in the Experimental section in the Supporting Information and simplified in Figure S1 (Supporting Information). Moreover, it is important to mention that, first, we conducted an optimization process to the devices through varying the thicknesses of the PEDOT:PSS, PM6:Y7, and PDINO layers (see details in the Figure S2 and Table S1, Supporting Information). Upon the mentioned optimization process in the SI, we depicted that the better performance was recorded for D8 through the proper optimization of the PM6:Y7 absorber active layer thickness along with the cathode interfacial layer thickness of PDINO. Then, to investigate the reason behind the enhanced J_{SC}, we focused on conducting a comparative insights on the morphological, optical, optoelectronic, electrical properties and related charge recombination dynamics between the pristine (non-treated-W/O Pre-TT) and the Pre-TT treated (Pre-TT) based devices of D1 (nonoptimized) and D8 (champion optimized) based devices. We examined the devices via current density voltage (J–V) under different illumination intensities, at 0.1, 1, 10, 16, 25, 50, 80, and 100 mW cm^{-2}, external quantum efficiency (EQE), mobility measurements, charge extraction (CE), and transient photovoltage/photocurrent (TPV/TPC) techniques. Furthermore, impedance spectroscopy (IS) measurements were performed through capacitance–voltage (CV) and capacitance-frequency (Cf) to understand the device behavior dependency on the Pre-TT approach.

Moreover, to confirm the high performance presented by our devices, we remeasured some devices such as D2 and D3 in the ICIQ facilities which exhibited quite similar performance as listed in Table S1 (Supporting Information), labeled as D2-ICIQ and D3-ICIQ.

2. Results and Discussions

2.1. Device Performance

The molecular structure of the PM6 polymer donor and Y7 non-fullerene acceptor with their corresponding energy band cascade of the conventional device structure are demonstrated in Figure 1. To evaluate the photovoltaic performance of the nonoptimized D1 and optimized D8 based devices, current density–voltage (J–V) characteristics under AM 1.5G illumination conditions were performed as shown in **Figure 2**a, the detailed statistic performance parameters were listed in **Table 1** and the photovoltaic PCE % statistics diagrams in Figure S3 (Supporting Information). The nonoptimized pristine NF-OPVs of Device 1 (D1-W/O Pre-TT) exhibited a maximum PCE of 13.94%, with a V_{OC} of 0.83 V, short circuit current density (J_{SC}) of 26.06 mA cm^{-2}, fill factor (FF) of 0.65, series and shunt resistances (R_S and R_{Sh}) of 0.98, and 473 Ω cm^2, respectively. For the nonoptimized Per-TT based devices (D1-Pre-TT), the J_{SC} and PCE were remarkably enhanced to 31.56 mA cm^{-2} and 15.04%, respectively, while the FF, R_{Sh} and V_{OC} were slightly diminished to 0.60, 315 Ω cm^2, and 0.81 V, respectively as listed

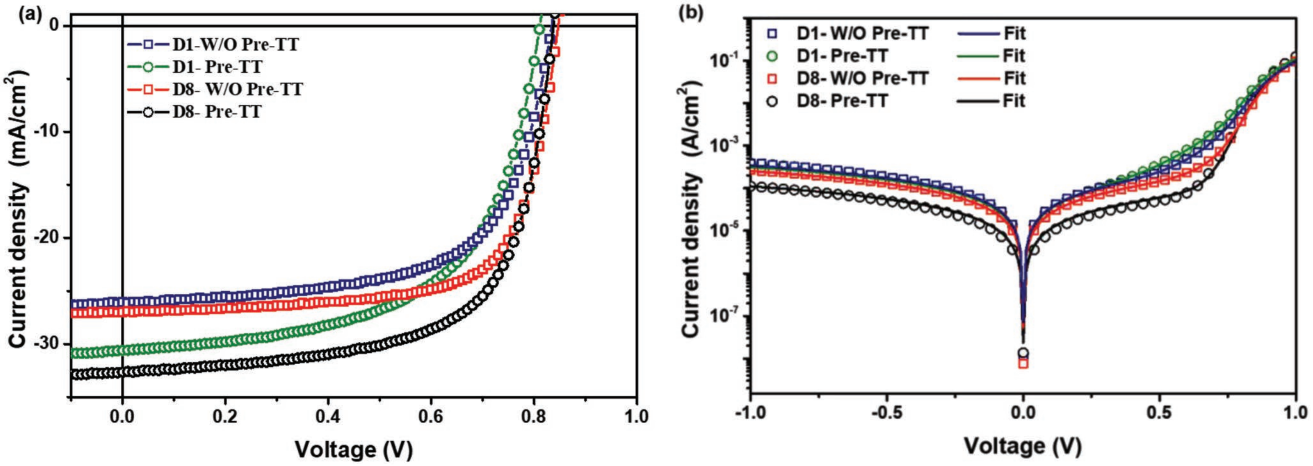

Figure 2. *J–V* characteristic curves of the pristine and the Pre-TT NF-OPVs of D1 and D8 a) under Illumination (AM 1.5 G), b) at dark condition (symbols for experimental data and the lines for the fitting).

in Table 1. Furthermore, the pristine-based devices of D8-W/O Pre-TT showed PCE of 16.07% with V_{OC} of 0.85 V, J_{SC} of 26.98 mA cm^{-2}, FF of 0.70, R_S, and R_{Sh} of 1.45 and 724 Ω cm^2, respectively consistent with the reported results.[5,19,21] Interestingly, the Pre-TT D8 devices (D8-Pre-TT) obtained extraordinary increase in the J_{SC} of 32.65 mA cm^{-2} and in turn the PCE were highly improved to 17.92% (see Table 1). However, the V_{OC} was the same (0.85 V), but the FF and R_S were slightly decreased to 1.13 Ω cm^2 and 0.66, respectively, as well as the R_{Sh} to 372 Ω cm^2. Thus, The Pre-TT devices of both D1 and D8 demonstrate slight decrease in their FF values and inconspicuous in their V_{OC} values as presented in Figure S4a (Supporting Information). This trivial change in the FF might correlate with the decline in the shunt resistances (R_{Sh}) of the Pre-TT, as displayed in Table 1. However, both Pre-TT device types (D1-nonoptimized and D8-optimized) exhibited a remarkable enhancement in their PCEs upon the great improvement in their J_{SC} values as presented in Figure S4b (Supporting Information). Hence, it is worth to mention that the strategies to optimize one parameter might oppositely affect another one, making it challenging to optimize the entire parameters at the same time. Therefore, even we got higher J_{SC} and PCE, that sacrifices with bit diminishing the FF as previously reported in Cui et al.[4] and Yuan[19] works. Overall, an outstanding J_{SC} value of 32.65 mA cm^{-2} is recorded for the D8 Pre-TT optimized based devices, which represent the top result for the nonfullerene OPVs devices as it is higher than the recently reported results in the literature[5,39–41]using the same active blend.

For further investigation of the Pre-TT NF-OPVs, we performed the *J–V* characteristic for the pristine and the treated devices in dark condition as shown in Figure 2b. On one hand, the highest leakage current was obtained from the thicker absorber active layer in Device 1 (D1-150 nm) showing a high shunt, possibly recognized as “induced shunts” that is responsible for diminishing the charge carrier at the interface.[42] This attitude might explain the lowest FF along with the PCE for these devices (D1), in contrast to the optimized D8 devices (100 nm), listed in Table 1. On the other hand, we found that the Pre-TT devices (of both D1 and D8) present almost one order of magnitude lower leakage current under the reverse bias conditions as compared to the pristine ones, indicating a higher shunt resistance.[43] Such behavior reveals the enhancement in the J_{SC} [43,44] of the Pre-TT devices than the pristine cells. Furthermore, to gain more insights we fitted the experimental data of the *J–V* at dark conditions through operating 2 diodes equivalent circuit model to calculate the series resistance (R_S) and shunt resistance (R_{Sh}) as demonstrated in Figure S5 (Supporting Information). Where the symbols in Figure 2b referred

Table 1. Main performance parameters of the pristine and the Pre-TT fabricated D1 and D8 NF-OPVs (All the devices were measured under standard conditions (100 mW cm^{-2} simulator irradiation at AM 1.5G) and the average parameters were calculated from minimum of nine fabricated devices for each configuration).

Device	V_{OC} (V)	J_{SC} [mA cm^{-2}]	FF	PCE [%]	R_S [Ω cm^2]	R_{Sh} [Ω cm^2]
D1-W/O Pre-TT	0.83	26.06	0.65	13.94	0.98	473
	0.82 ± 0.01	27.25 ± 2.12	0.62 ± 0.02	13.53 ± 0.60	1.26 ± 0.62	397 ± 76
D1- Pre-TT	0.81	31.56	0.60	15.04	0.94	315
	0.80 ± 0.01	29.69 ± 1.87	0.61 ± 0.02	14.20 ± 0.84	0.81 ± 0.13	305 ± 10
D8-W/O Pre-TT	0.85	26.98	0.70	16.07	1.45	424
	0.84 ± 0.01	27.15 ± 1.82	0.69 ± 0.02	15.82 ± 0.61	1.18 ± 0.27	625 ± 99
D8- Pre-TT	0.85	32.65	0.66	17.92	1.13	372
	0.84 ± 0.01	31.44 ± 1.36	0.65 ± 0.06	17.61 ± 0.31	0.80 ± 0.52	374 ± 29

to the experimental data and the lines to the fitting values that are listed in Table S2 (Supporting Information). The fitting data showed an exponential region ($0.65 < V$ (V) < 0.85) with higher ideality factor ($n1$) values of 2.01 and 1.27 for the pristine devices of D1 W/O Pre-TT and D8 W/O Pre-TT, respectively, in comparison to the $n1$ of 1.35 and 1.15 for the D1 Pre-TT and D8 Pre-T, respectively. Moreover, the fitted values in Table S2 (Supporting Information) depicted a noticeable increase in the R_{sh} values for the Pre-TT D1 (3.2×10^3 Ω cm^2) and D8 devices (1.1×10^4 Ω cm^2) in comparison to those for the pristine cells (R_{Sh} of D1 W/O Pre-TT = 2.9×10^3 Ω cm^2 and R_{Sh} of D8 W/O Pre-TT = 3.9×10^3 Ω cm^2). These obtained results explain the diminishing of the leakage current behavior observed for the Pre-TT devices,[42] especially for the optimized D8 Pre-TT that possessed the champion performance. This variation in leakage current in the fabricated devices is common in OPVs due to many reasons and is directly related to the thickness, quality and morphology of the films.[45,46]

Figure 3a displays the external quantum efficiency (EQE) response with AM 1.5G reference spectrum of the pristine and Pre-TT devices. It can be noticed that the entire devices have a similar wavelength range of a broad photoresponses from 300 to 900 nm, indicating the contribution of both donor and NF acceptor to the overall generated photocurrent. We can see that the EQE intensity at short wavelengths range of 300–450 nm is lower due to the limited absorption of the polymer donor in this region.[4,11] However, the EQE spectra from 450 to 800 nm exhibited stronger photoresponses with a maximum plateau achieving around 80% for the pristine devices (D1-W/O Pre-TT and D8-W/O Pre-TT), around 90% for D1-Pre-TT and > 95% for D8-Pre-TT. In addition, we calculated the integrated J_{SC} from the EQE spectra (listed in Table S3, Supporting Information) which are consistent with the values obtained from the J–V listed in Table 1. Interestingly, the observed EQE response provides good proof for the extraordinary high current generated from the devices fabricated with Pre-TT approach. It is worth noting that in the absorption range of 450–850 nm, the pristine-based devices showed different EQE spectral shape response than Pre-TT based ones. However, it is well known that optical interference and parasitic absorbance in nonactive layers provide a pronounced effect on the shape of the measured EQE as a passive optical effect. But, the BHJ layer thickness (and therefore the resulting film roughness) has a first-order effect on the spectral dependence of the EQE.[47] Hence, we

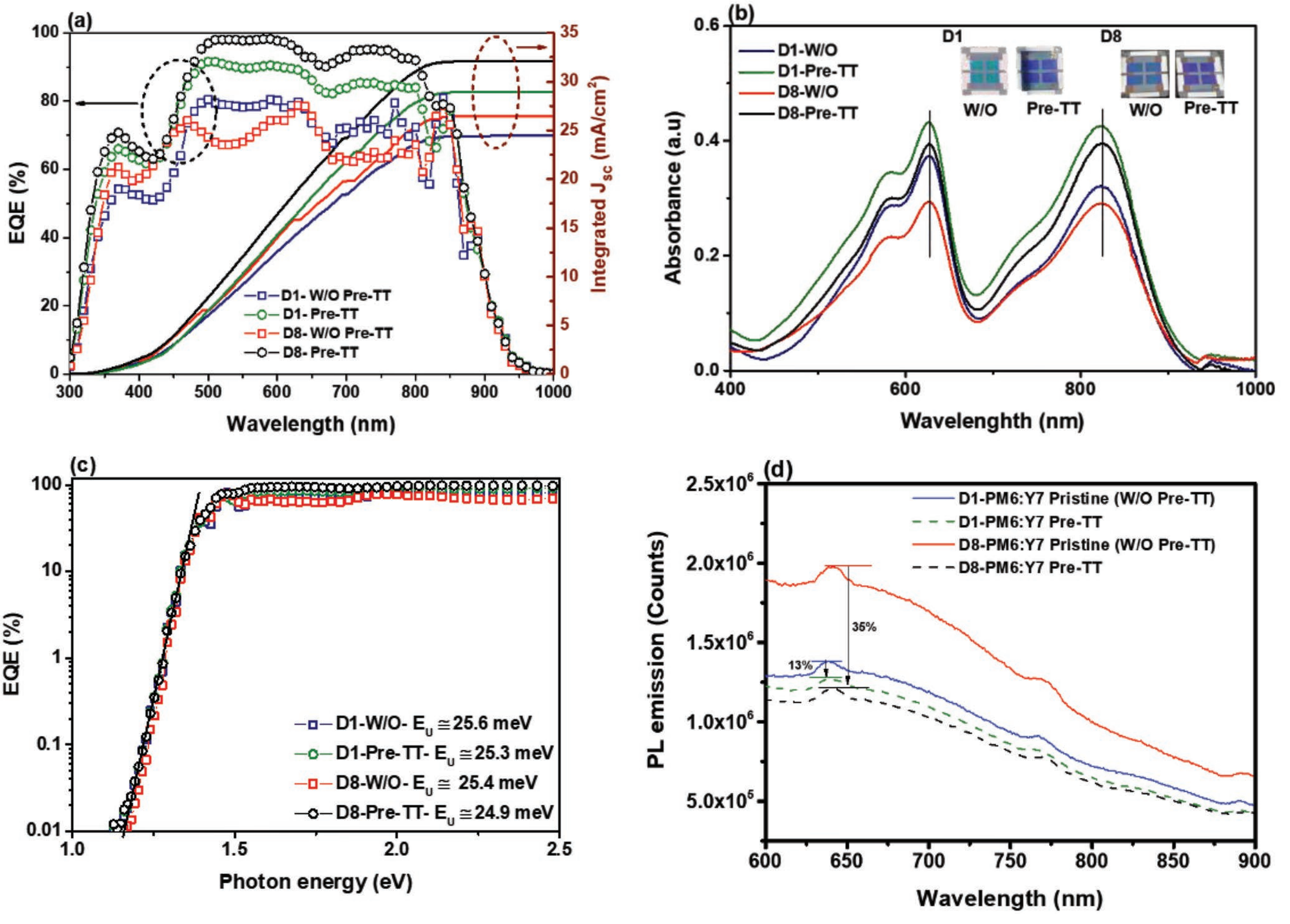

Figure 3. a) EQE spectra (left axis) and the integrated short circuit current (right axis) of the NF-OPVs pristine and Pre-TT of D1 and D8 devices, b) UV–vis absorption spectra of the ITO/PEDOT:PSS/PM6:Y7 structure based on D1 and D8 with an inset photo of the fabricated devices. c) EQE versus photon energy of the pristine and PreTT NF-OPVs devices, and d) PL spectra of the pristine and the Pre-TT pure blend films over the PEDOT:PSS.

suggested that it might be attributed to the higher roughness observed for the pristine-based films as will be explained in the Section 2.5. Thus, in our case different microstructures reveal a more pronounced influence on the EQE spectral shape which is provided upon thickness variation and Pre-TT factors. Therefore, it is a foremost to obtain the internal quantum efficiency response (we will return to this measurement in the following parts) since it neglects the multilayer optical phenomena and the parasitic absorptions in nonactive layers such as ITO, PEDOT:PSS, as ascribed by Armin et al.[48]

For further investigation related to the phenomena beyond the improvement of the generated current density for the Pre-TT devices, we measured the UV–vis absorption spectra of the ITO/PEDOT:PSS/PM6:Y7 structure for the pristine and the Pre-TT based films as shown in Figure 3b. We can explicitly see the enhancement in the light absorption of the D1 and D8 Pre-TT based films without any bathochromic shift. Furthermore, the inset images in Figure 3b show the real photo of the pristine and Pre-TT devices. The color of the active blend turns to darker upon the Pre-TT step in both D1 and D8 devices, showing the potential to improve the photon harvesting of the host blend in the Pre-TT based devices (D1-Pre-TT and D8-Pre-TT) which in turn enhances the generated J_{SC} as confirmed by the previously discussed *J*–*V* curves. This behavior was previously reported by Tang,[49] ascribing that the improved absorption was attributed to the refining of the active layer morphology upon the Pre-TT (will be discussed in details in the Section 2.5.).

In addition, it is worth to mention that the V_{OC} values of the corresponding pristine and Pre-TT devices (listed in Table 1) did not show a remarkable change that greatly matches the consistency of the PM6:Y7 peak position in Figure 3b. Accordingly, the enhancement in the EQE spectra due to the Pre-TT approach might be attributed to the modulation of the absorption energy in the active blend.[11] This behavior perfectly matches with Liu et al. research work.[11]

Furthermore, to evaluate the charge generation, extraction, and collection processes of the devices within the photoactive layer, taking into account the recombination losses that might take place in the based devices. We calculated the internal quantum efficiency-IQE, following the correlation as described by Forrest[50] and Armin et al.[48] that expressed as $\eta_{IQE} = \eta_{EQE}/\eta_A$, where η_{IQE} is the fractional internal quantum efficiency presented by the ratio of the number of the collected charges to the photons absorbed by the junction and η_A reveals the absorbed incident light amount by the photoactive layer. Hence, the IQE represents the photovoltaics response normalized by the number of photons actually absorbed by the photoactive layer and thus provides information about the behavior of the charge generation (exciton dissociation, charge transfer) and collection processes.[50] Figure S6 (Supporting Information) displays the IQE of the pristine and Pre-TT based devices. The overall IQE intensities of the Pre-TT based devices are higher than the corresponding pristine ones. However, the contributed efficiency was varied from both donor and acceptor regions. Where, high IQE values in the range of 400 to 550 nm were 99.68%, 92.12%, 90.06%, and 88.86% for the D8-Pre-TT, D8-W/O Pre-TT, D1-Pre-TT, and D1- W/O Pe-TT, respectively, and 52.42%, 35.52%, 42.82%, and 25.03%, respectively, in the range of 650 to 800 nm. The IQE >900 nm has been omitted regarding the absorption falling edge at these wavelengths. Accordingly, it can be exhibited that the pristine-based devices possessed lower IQE intensities than the Pre-TT ones, revealing the less efficient exciton dissociation and free charge extraction. In contrast to the Pre-TT-based device, specifying D8-Pre-TT optimized devices, suggesting that a significantly larger portion of the absorbed photons are converted to free charge carriers which are then collected by the corresponding electrodes which greatly matches with their superior EQE response (Figure 3a) and their J_{SC} values (Table 1). This might be facilitated by the fine-tuning of the Pre-TT based blend morphology (in the Section 2.5.), revealing that excitons generated can therefore reach the D/A interface and efficiently dissociate, resulting in high IQE values.

Interestingly, Figure 3c showed the logarithmic scale of the EQE versus the photon energy to confirm the effect of the Pre-TT step on the optical properties of the active blend film using the Urbach rule as follows:[11,51]

$$\alpha(E) = \alpha_0\, e^{(E-E_g)/E_U} \tag{1}$$

where, α (*E*) is the optical absorption coefficient, α_0 is the optical absorption coefficient at the band edge, *E* is the photon energy and E_U is the Urbach energy. The photocurrent spectrum response of the entire devices is up to 1.4 eV that relates to the same photoactive blend of PM6:Y7.[11] Therefore, the higher photocurrent response of the devices is more likely correlated to the excitation of the active blend, and the lower photocurrent response than 1.4 eV is more attributed to the charge transfer states.[52,53] Accordingly, the Urbach energy of the devices was defined with the absorption tail (known as Urbach tail) below 1.4 eV as described in Equation (1). Hence, the E_U value represents the density of state distribution that explains the energetic disorder in the molecular orbitals,[51] which is considered as a valuable parameter revealing the influence of all possible defects.[54] Upon this context, the smaller E_U value corresponds the abrupt band edge.[11] The extracted E_U values of the devices are quite a similarity (around 25 meV) which is comparable to the thermal energy k_BT (25.8 meV) at room temperature.[51] However, they follow the same trend of devices performance (as listed in the inset of Figure 3**c**), where lower E_U values were exhibited for the Pre-TT devices that possessed better performance than the pristine ones. This obtained behavior from the Pre-TT samples might be due to diminishing the energetic disorder in the active blend as revealed by the morphological characteristics discussed in the following sections and in turn improving its optical properties.[11] Furthermore, these observations were verified by the optimized D8-Pre-TT devices which present the lowest E_U value, indicating the lowest energetic disorder that originates the superior device performance via declining the density of state distributions that in turn retard decreasing the recombination (Table 1).[55,56]

Moreover, to examine the exciton dissociation behavior and the charge transfer processes, we performed photoluminescence (PL) measurements of the pristine and the Pre-TT pure blend films over the PEDOT:PSS layer (Figure 3d). To get a fair comparison, we used the same films measured for the absorption spectra and by using the same excitation wavelength

(635 nm). The observed results indicate that the PL spectra of pristine films present higher intensity than the Pre-TT ones, where the PL response is quenched by 13% and 35% for D1 Pre-TT and D8 Pre-TT, respectively. This remarkable PL quench of the Pre-TT films, especially for the optimized D8 Pre-TT film, implies an efficient charge transfer at the interfaces of the PEDOT:PSS/PM6:Y7, resulting in higher generated current.[57,58] The PL results follow the same trend of the J_{SC} values of the corresponding based devices obtained (Table 1) as well as their EQE response in Figure 3a. Same response was further noticed for the PEDOT:PSS/PM6 films performed as a reference of D1 and D8 pristine and Pre-TT films as shown in Figure S7a,b (Supporting Information), respectively. Interestingly, same behavior was reported by F. Jin et al. upon the thermal annealing effect.[32]

2.2. Carrer Dynamics

In order to better understand the improvement of the treated devices upon the effect of the Pre-TT approach, we further measured the carriers dynamics of the devices via the advanced photoinduced spectroscopic techniques through charge extraction (CE), transient photovoltage (TPV) and transient photocurrent (TPC), evaluating the variation of charge transport, accumulation, and recombination that take place in the devices (see Figure S8, Supporting Information for more information).[59,60] **Figure 4**a presents the photogenerated charge density of the pristine and Pre-TT devices under different light bias from 1 Sun to dark, providing different V_{OC} values. The symbols indicate the geometrical and the chemical capacitance or in other words, the charges accumulated at the interfaces and in the bulk, respectively. Consequently, to disclose a clear interpretation of the obtained data, we subtracted the geometrical capacitance obtaining the solid lines at the bottom of Figure 4a, revealing the charges presented at the bulk.[61] We noticed that the Pre-TT devices (D1-Pre-TT and D8 Pre-TT) exhibited higher number of charges (solid lines) compared to the pristine ones, describing the higher J_{SC} values obtained by J–V characteristics (Figure 2a) of the Pre-TT devices (Table 1). Furthermore, all devices present a similar slope at 0.4–0.6 V range, indicating insignificant differences in the energy level position of the pristine devices and their corresponding Pre-TT cells,[62,63] clarifying the consistency of their V_{OC} values. Moreover, Figure S9 (Supporting Information) shows the charge carrier lifetimes scale with voltage, extracted from the TPV decays. The recombination was faster for the pristine devices, confirming their lower J_{SC} as well as PCE. However, for a proper comparison, Figure 4b displays carrier recombination lifetime (tau) versus charge density to evaluate the carrier recombination dependence on the charges of the corresponding devices. We observed that, for the same number of charges, the recombination is slightly faster for the pristine devices. Hence, it is worth noting that the Pre-TT NF-OPVs demonstrated more charge generation which neither lead to recombination behavior nor affecting V_{oc}, exhibiting better performance than their pristine counterparts. This behavior might be attributed to the presence of defect states[60,63,64] in the pristine devices that are efficiently reduced by the Pre-TT approach. These results agree well with the PL characteristics (Figure 3d) and consequently better J_{SC} along with the overall enhanced performance of the Pre-TT devices.

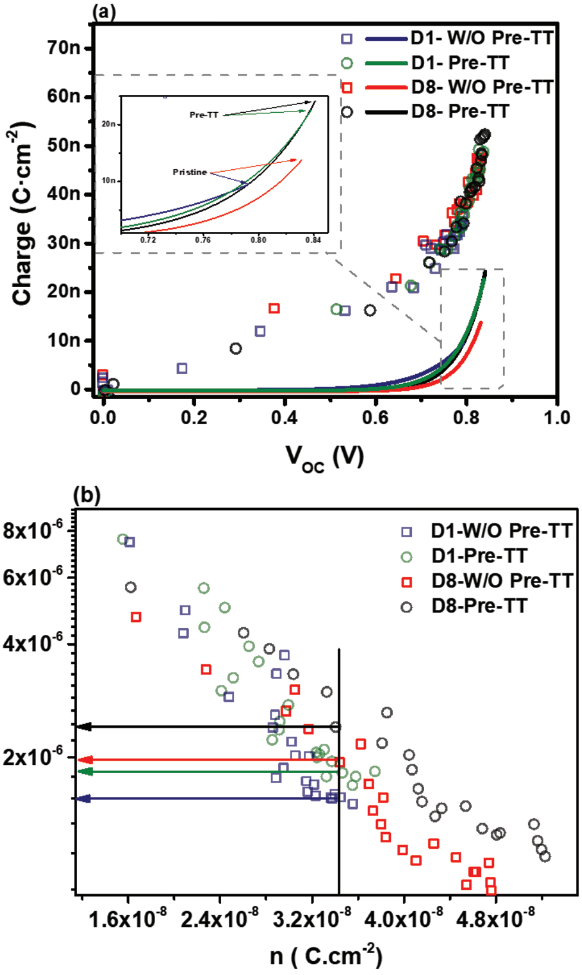

Figure 4. a) Charge measured at different light biases for the pristine and Pre-TT devices. The symbols correspond to both geometrical capacitance and chemical capacitance. The solid lines at the bottom represent only the exponential part: $y = Be^{Cx}$ (chemical capacitance) after subtraction of the geometrical capacitance, b) charge measured by CE versus the carrier lifetime obtained via TPV for the pristine and Pre-TT devices.

Furthermore, we noticed that the CE and TPV characteristics did not demonstrate a significant difference regarding the recombination behavior within our devices. Therefore, we further investigated the nature of the recombination occurred for the fabricated pristine and the Pre-TT devices through studying the dependence of J_{SC} and V_{OC} on the incident light intensity (P_{light})[65] under AM 1.5 G illumination condition as shown in **Figure 5**, gaining more insights to understand the improvement of the J_{SC} for the Pre-TT devices.

Figure 5a displays the J_{SC} power law dependence on the light intensity (P_{light}) that following the proportional relation of $J_{SC}\ \alpha\ P_{light}^{S_1}$ in principle, where S_1 is the exponential factor that represents the bimolecular recombination in devices along with the ability of extracting the free carries through the corresponding electrodes.[5,65,66] Basically, under short circuit condition, the S_1 value is unity when there is negligible bimolecular

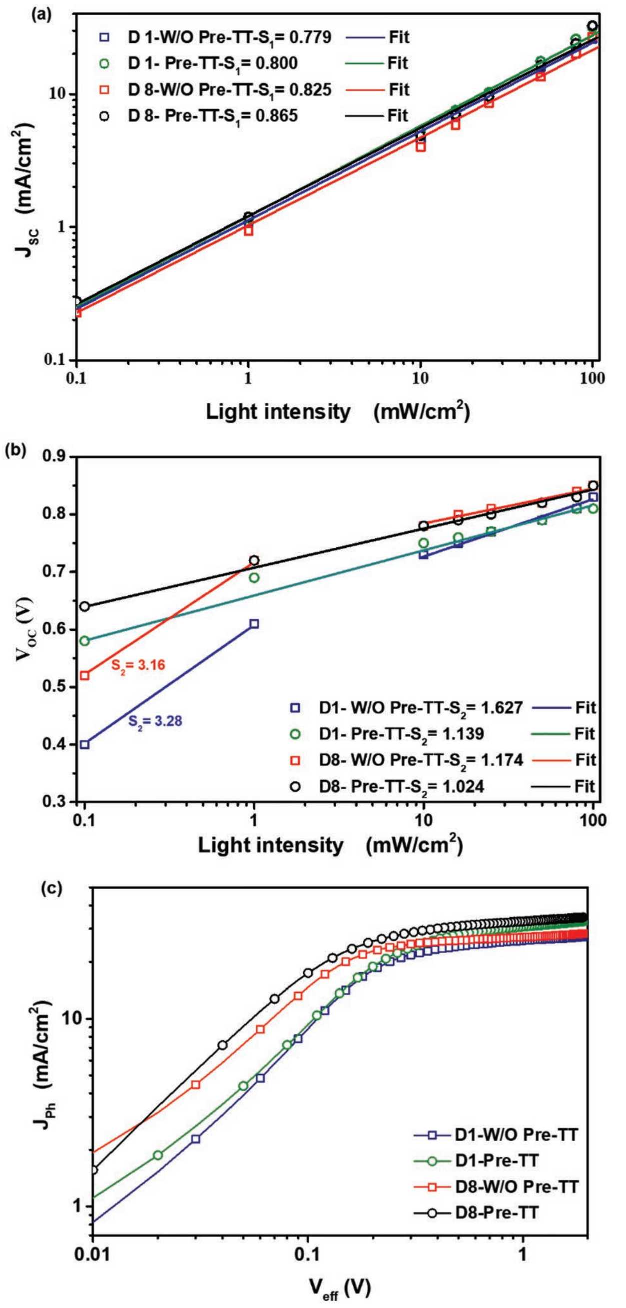

Figure 5. a) J_{SC} and b) V_{OC} versus the light intensity, symbols refer the experimental data and lines for the fitted data, c) J_{Ph} versus V_{eff} characteristics of the pristine and Pre-TT of D1 and D8 NF-OPVs devices.

recombination appears in the donor/acceptor blend films and less than 1 in case of the presence of the bimolecular recombination.[67,68] The fitted values of S_1 were 0.799, 0.800, 0.825 and 0.865 for D1-W/O Pre-TT, D1-Pre-TT, D8-W/O Pre-TT, and D8-Pre-TT, respectively. As a sequence, the obtained results showed a linear behavior which indicate a presence of bimolecular recombination for the entire devices,[69,66] as a significant loss mechanism in the OPVs.[70]

We noticed that both Pre-TT devices possessed S_1 values closer to 1 in comparison to the corresponding pristine devices. Interestingly, the closest S_1 value to 1 was obtained for the optimized D8 Pre-TT which might reflect the less contribution of non-geminate charge recombination.[68,71] This behavior is highly matched with the lower leakage current (Figure 2b) and the highest J_{SC} regarding the D8-Pre-TT devices in the J–V characteristics (Table 1).

Moreover, it is well known that the ΔV_{OC} dependence of the $\Delta \ln\,(P_{light})$ has been effectively used to identify the presence of the trap-assisted SRH recombination.[45,70] Hence, Figure 5b illustrates the logarithmic dependence of the V_{OC} on the P_{light} of the fabricated devices, representing the diode Equation (2) of

$$V_{OC}\;\alpha\;S_2\left(\frac{k_BT}{q}\right)Ln\left(P_{light}\right)\alpha\;n_{id}\left(\frac{k_BT}{q}\right)Ln\left(J_{SC}\right) \tag{2}$$

where n_{id} is the ideality factor of the diode ($n_{id} = S_2/S_1$), k_B is the Boltzmann constant, T is the temperature, and q is the elementary charge. The n_{id} value specifies that the bimolecular recombination is the exclusive form of recombination in the OPV devices when it close to 1,[67] while higher n_{id} value than 1 designates the presence of the trap assisted recombination mechanisms SRH.,[72,68] The values of S_2 were extracted by fitting Equation (2), obtaining values of 1.627, 1.139, 1.174, and 1.024 that leads to n_{id} values of 2.089, 1.418, 1.401, and 1.184 for the based devices of D1-W/O Pre-TT, D1-Pre-TT, D8-W/O Pre-TT, and D8-Pre-TT, respectively. First, it can be noticed that the n_{id} values for D1 are higher than those for D8 which might be related to the nonoptimized PM6:Y7 thickness in the D1-based devices, explaining the recombination observed in these devices. Second, the Pre-TT based devices showed n_{id} values close to 1 in comparison to both pristine nontreated devices. These observed results suggest that the Pre-TT approach suppresses the trap-assisted recombination mechanisms, which may reflect the efficient charge transport and extraction of the devices.[72,68] It is worth to mention that this behavior might explain the previously observed lower E_U values for the Pre-TT devices along with confirming the higher J_{SC} values, EQE, and PL responses in comparison to the pristine devices.

Moreover, it was interesting to detect that at low light intensities (<10 mW cm^{-2}), the pristine devices behaved differently than the pre-TT ones as shown in Figure 5b. Where the pristine D1-W/O Pre-TT and D8-W/O Pre-TT devices exhibited higher S_2 values of 3.28 and 3.16, respectively, and in turn a n_{id} values of 4.21 and 3.98, respectively. It is well known that at low voltage and low light intensities (<10 mW cm^{-2}), the region is governed by R_{Sh}, exhibiting shunt behavior that can be clearly identified as a rapid voltage drop.[73,74] Then after 10 mW cm^{-2} the diode is entering its real diffusion current dominated regime, where ideality factor can be determined as ascribed by Tvingstedt and Deibel.[74] Accordingly, the high n_{id} values and the different linear behavior at low P_{light} of the pristine-based devices might be attributed to the pronounced shunt recombination loss mechanisms, preventing a sufficient carrier density to be maintained.[74] and being dominated by trap-assisted recombination mechanism SRH.[70] In contrast to the Pre-TT devices (D1 and D8) that have no remarkable shunt paths across their PN junction as well as less nonideal recombination behavior is taking place,[71] possessing mainly bimolecular recombination form under open circuit and short circuit conditions. Specifically, the D8-Pre-TT-based devices which showed the champion n_{id} value (closest to 1), provided a lower slope which implies trap-free recombination behavior.[65,75] Then, it might be the main reason of their superior performance of J_{SC} and PCE over the other devices. Furthermore, it was surprising to find that the obtained n_{id} values from the V_{OC} and P_{light} dependency were in excellent agreement with the obtained n_1 values from the dark J–V characteristics discussed previously (Table S2, Supporting Information).

Moreover, the dependence of the photocurrent density (J_{Ph}) on the effective voltage (V_{eff}) was calculated to depict the exciton dissociation probabilities (P_{diss}), maximum amount of absorbed photons that leads to the dissociation and generation of free carriers (G_{max}) and the generation rate (G_{rat}) of the free charge carriers for the pristine and the Pre-TT NF-OPVs.[43,76,77] The J_{Ph} is defined as J_L–J_D, where the J_L and J_D are the current densities under illumination and at dark, respectively. V_{eff} is described as V_O -V, where V_O is the voltage when $J_{Ph} = 0$ and V is the applied voltage,[78,67,79] We calculated the values of the G_{max}, P_{diss}, and G_{rat} using the following reference equations of[76,77,79,80] $G_{max} = J_{sat}/qL$, $P_{diss} = J_{SC}/J_{sat}$, and $G_{rat} = P_{diss}\ G_{max}$, where J_{sat} is the saturation current density at 0.2 V, q is the elementary charge and L is the thickness of the blend film.

From the double logarithmic scale plot of J_{ph} versus V_{eff} in Figure 5c, we disclosed that almost all photogenerated charge carriers were collected at high field of $V_{eff} > 0.2$ V, where at low field of $V_{eff} < 0.2$ V the J_{ph} of the devices was increasing linearly. Then, it saturates by increasing the $V_{eff} > 0.2$ V revealing an efficient charge carrier separation.[76] Hence, from the calculated J_{sat} in Figure 5c, we can observe that the Pre-TT based devices (D1-Pre-TT and D8-Pre-TT) manifest better charge carriers separation through the interfaces of the active layer blend,[76,67] more than the pristine devices (D1-W/O Pre-TT and D8- W/O Pre-TT). Then, Table S4 (Supporting Information) summarizes the optoelectronic parameters calculated from the J_{ph} versus V_{eff} curves. The values of the G_{max} were 1.17×10^{28} and 1.76×10^{28} m^{-3} s^{-1} for the pristine D1-W/O Pre-TT and D8-W/O Pre-TT devices, respectively, while the G_{max} values for the Pre-TT D1 and D8 devices were 1.37×10^{28} and 2.09×10^{28} m^{-3} s^{-1}, respectively. It is worth to mention that the Pre-TT devices showed a noticeable increase in the G_{max} rather than the pristine devices, representing the excellent energy harvesting due to the efficient exciton generation in the corresponding devices.[77,79] Moreover, these observed results matched with the higher G_{rat} values of Pre-TT devices in comparison to the pristine ones (listed in Table S4, Supporting Information), confirming that the photogenerated excitons were more efficiently dissociated into free carriers owing to the Pre-TT post treatment approach. Furthermore, the P_{diss} values of the fabricated devices followed the same trend of the other parameters, being as D8-Pre-TT (97.46%) > D8-W/O-Pre-TT (95.56%) and D1-Pre-TT (93.02%) > D1-W/O-Pre-TT (92.36%), which is greatly complies the obtained n_{id} values of the corresponding devices discussed previously.

To validate the P_{diss} values obtained from Figure 5c, we plotted the J_{ph} to their saturation value ($qG_{max}L$ in Equation 2) as shown in Figure S10 (Supporting Information) for the NF-OPVs. The photocurrent indicates the dissociation efficiency in the saturation region at $V_{eff} > 0.2$ V.[26,67] It shows that applying the Pre-TT approach to the films leads to an enhancement in the dissociation efficiency in the V_{eff} region < 0.2 V which in accordance with the obtained P_{diss} values. In addition, the most significant difference appeared for D1 and D8 at $V_{eff} < 0.2$ in Figure 5 and Figure S10 (Supporting Information) is mainly due to the FF as a result of the thickness variation in the PM6:Y7 film in the representative devices which in turn affect the recombination and the P_{diss} within the devices. Accordingly, greater P_{diss} values correlate with the lower recombination as presented by the D8 based NF-OPVs, consisting with their extraordinary enhanced J_{SC} values.

2.3. Charge Mobility

Furthermore, the space-charge-limited current (SCLC) measurements were probed to calculate the e/h mobilities, the trapped filled limit voltage (V_{TFL}) and the trap density (N_{trap}) of the pristine and the treated blend-based films of D1- W/O Pre-TT, D1-Pre-TT, D8-W/O Pre-TT, and D8-Pre-TT) as explained in Figure S11 (Supporting Information) with the calculation details in the Supporting Information. The tested hole-only devices are presented as a sandwich capacitor-like architecture of ITO/PEDOT:PSS/PM6:Y7/Au and the electron-only devices with structure of ITO/ZnO/ PM6:Y7/PDINO/Ag in the dark as illustrated in Figure S12a,b (Supporting Information), respectively. **Figure 6**a displays the SCLC curves of the electron-only devices of the pristine and Pre-TT devices. The electron mobility values (μ_e) of the fabricated devices were calculated following the Mott- Gurney model[81,82] of $J_{SCLC} = 9/8\varepsilon_0\varepsilon_r\mu_{SCLC}\ V^2\ L^{-3}$. We depicted that the μ_e values of the pristine D1-W/O Pre-TT and D8-W/O Pre-TT were 9.31×10^{-4} and 7.97×10^{-4} cm^2 V^{-1} S^{-1}, respectively, while the μ_e values of the Pre-TT devices were D1-Pre-TT = 3.51×10^{-3} cm^2 V^{-1} S^{-1} and μ_e of D8-Pre-TT = 3.72×10^{-3} cm^2 V^{-1} S^{-1}. Accordingly, we noticed that despite the blend thickness variation from 150 nm in D1 and 100 nm in D8 which did not express a noticeable effect on the μ_e same as found elsewhere[83] as we use the same blend ratio, but the Pre-TT devices provided a higher μ_e than the pristine ones.

Moreover, it is important to note that the μ_e values of the Pre-TT devices are about one order of magnitude higher than most of the other blends reported[84–86] as well as close to Tokmoldin work, explaining the same reason behind the high J_{SC} values obtained for their corresponding devices.[87] Moreover, by considering the thickness of the blend film for D1(150 nm) and D8 (100 nm), we found that the estimated values of the N_{trap} for the Pre-TT devices (D1- Pre-TT = 3.96×10^{15} cm^{-3} and D8- Pre-TT = 5.81×10^{15} cm^{-3}) were lower than the pristine ones (D1-W/O Pre-TT = 5.94×10^{15} cm^{-3} and D8-W/O Pre-TT = 10.11×10^{15} cm^{-3}) as explained in the Supporting Information and listed in Table S5 (Supporting Information), which showed an excellent match with the lower E_U values observed for the Pre-TT devices as aforementioned. Moreover, it is worth to mention that the values of the V_{TFL} were diminished for the Pre-TT devices, as listed in the inset of Figure 6a. This behavior indicates that the Pre-TT approach passivated the trap states of the treated devices, providing an enhanced path for an efficient

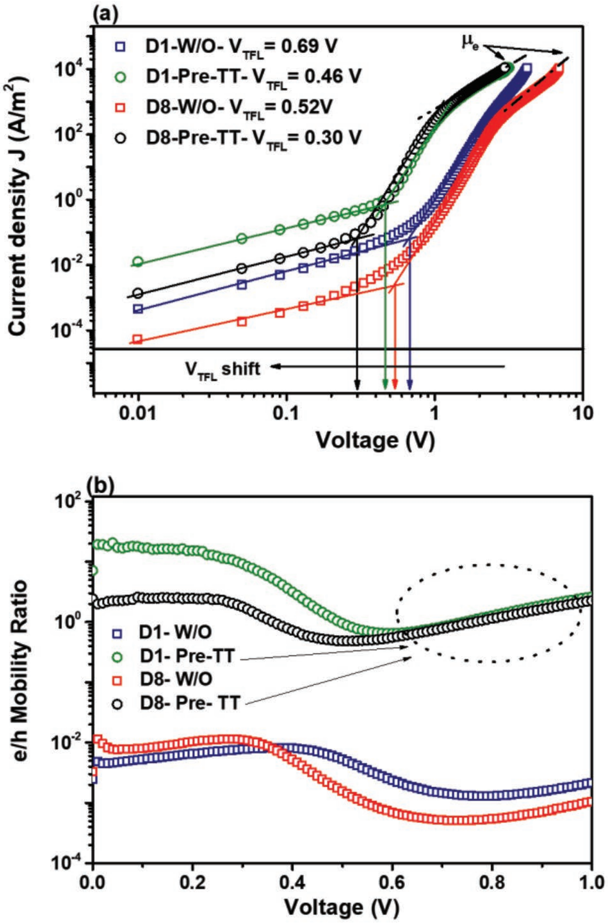

Figure 6. a) The SCLC curves of the electron-only pristine and Pre-TT devices, b) *e*/*h* mobility balance of pristine and Pre-TT devices.

charge carrier transfer and collection by suppressing the defect density and the recombination mechanisms.[81,82,88] That also explains their superior P_{diss}, $G_{\max}$, J_{SC} along with their boosting PCE in comparison to the pristine devices. Moreover, in order to confirm the charge trap density behavior in the pristine and the Pre-TT devices, the hole-only devices were also examined by the SCLC measurements, evaluating same previous observations of terminating V_{TFL} and the N_{trap} values for the Pre-TT devices as shown in Figure S13 and Table S6 (Supporting Information).

Furthermore, it is well known that the mobility balance (μ_e/μ_h) is a key factor governing the overall performance of the OPVs devices.[89] The unbalanced mobility leads to space charge formation along with significant recombination because in case of the unbalanced charge transport, the cells performance is mainly limited by the slower carrier, resulting in determination in the J_{SC} along with the PCE of the devices.[89,90] In contrast, the performance of the PV devices maximized when the μ_e/μ_h ratio is close to unity, meaning balanced carrier mobilities which are beneficial to enhance the charge transport and in turn the device performance.[61,89,91,92] Accordingly, we plot the logarithmic curve of the mobility balance (μ_e/μ_h) against the voltage as displayed in Figure 6b to estimate the μ_e/μ_h of the different devices. Our results presented that, at V_{OC}, the pristine devices showed μ_e/μ_h values of 4.0 and 2.3 for the D1-W/O Pre-TT and D8-W/O Pre-TT devices, respectively. This imbalanced carrier mobility might be detrimental to the overall charge collection,[61] revealing the drop of their J_{SC} and PCE values obtained (Table 1). On the contrary, well-balanced μ_e/μ_h of 1.4 and 1.3 were obtained for D1-Pre-TT and D8-Pre-TT NF-OPVs, respectively. Moreover, it was interesting to notice that at high voltage around the maximum power point voltage (V_{mpp}) and the V_{OC}, only the Pre-TT devices demonstrated the mobility balance close to one, in contrast to the pristine NF-OPVs, as can be seen in Figure S14 (Supporting Information). Consequently, the extraordinary enhancement in the J_{SC} and PCE values of the Pre-TT devices might be attributed to deteriorating the recombination mechanisms as well as ameliorative charge transport,[93] which as well revealed by the previously discussed characteristics. These results confirm that the Pre-TT approach has an effective influence to assist balancing the electron and hole transport. In addition, it was interesting to note that the devices performance increase as the balanced carrier mobility close to unity as clearly observed for the champion optimized D8-Pre-TT based devices. Accordingly, it was interesting to correlate that the more balanced *e*/*h* transport (Pre-TT devices) decreases the E_{U} values in combination with low SRH recombination represented by the high G_{rat} that might be the key parameters that led to a remarkable enhancement in the performance of the Pre-TT devices as further observed by Firdaus et al.[90] and Athanasopoulos et al.[94]

As an alternative way to interpret the obtained results, the diffusion length, (L_{d}) of the pristine and Pre-TT NF-OPVs can be calculated using the formula: $L_{\mathrm{d}} = \sqrt{\mu t \frac{T k_{\mathrm{B}}}{q}}$, where μ is mobility, and t is the carrier recombination lifetime (tau).

The tau values are extracted from the TPV measurements (Figure 4b) and the electron and hole mobility values obtained from SCLC measurements (Figure 6a and Figure S12, Supporting Information). We found that the estimate electron L_{d} values of the devices were 121 nm in D1-W/O Pre-TT, 128 nm in D1 Pre-TT, 139 nm in D8-W/O Pre-TT, and 156 nm in D8 Pre-TT devices. Moreover, the hole L_{d} values of the devices were 41 nm in D1-W/O Pre-TT, 44 nm in D1 Pre-TT, 48 nm in D8-W/O Pre-TT, and 54 nm in D8 Pre-TT devices. Hence, these rather higher estimated carrier diffusion length values in the Pre-TT devices in comparison to the pristine cells that may justify their observed better device performance, specifically, the high J_{SC} values[95] and especially for the D8- Pre-TT optimized devices.

2.4. Impedance Spectroscopy

Impedance spectroscopy (IS) characterization technique has been carried out as an insight analysis to study the effect of Pre-TT approach on the performance of the fabricated NF-OPVs. It is a powerful diagnostic technique for monitoring the recombination, carrier accumulation, and transport behavior of each layer within the OPVs.[60,96,97] It measures the phase shift and the amplitude of the current response obtained through applying an AC voltage to the devices at a given frequency range, which reveal different mechanisms taking place at various interfaces.[96,98]

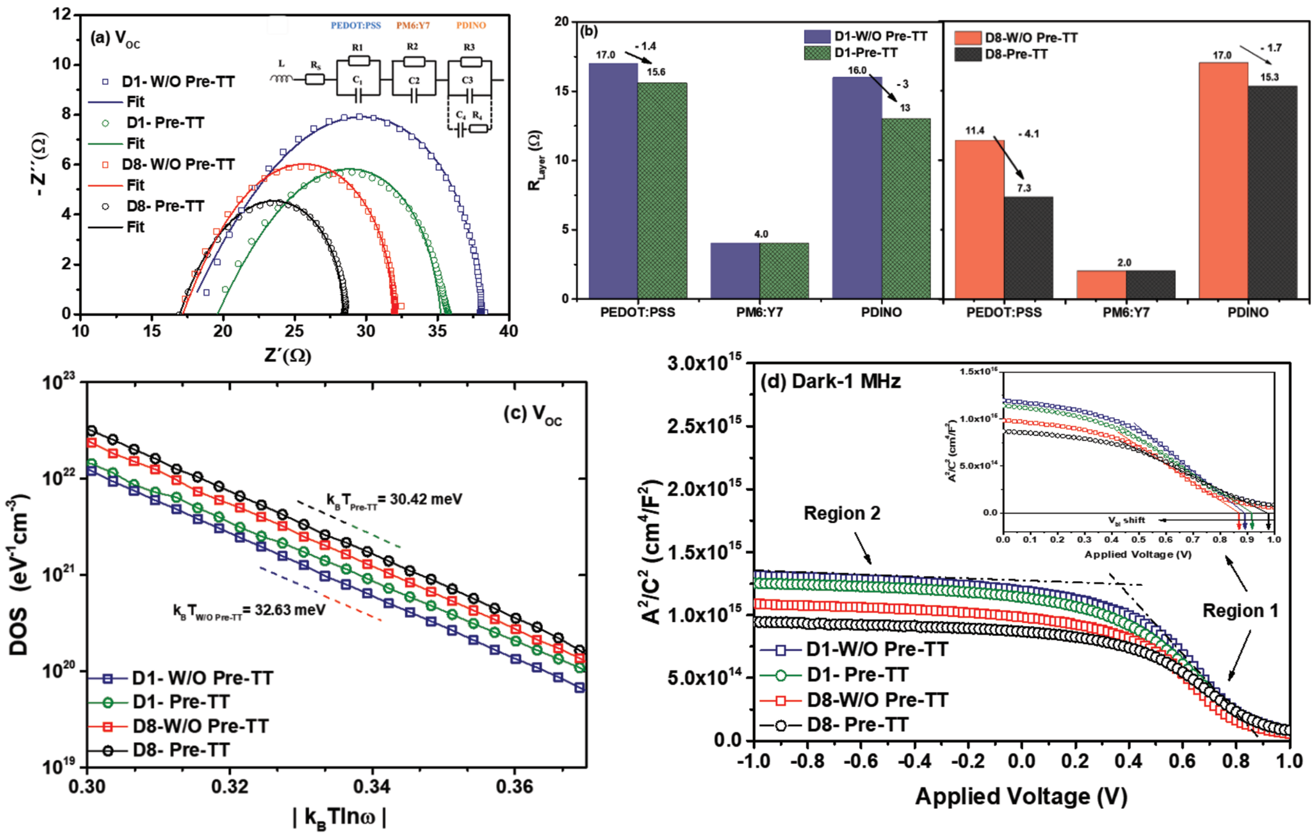

Figure 7. a) Cole–Cole plots at V_{OC} under AM 1.5G illumination, using symbols for the experimental data and the fitting results in solid lines by applying the inset equivalent circuit of Debye model, b) the resistance of each layer within the pristine and Pre-TT NF-OPVs of D1 and D8 c) DOS as function of $|k_BT\ln\omega|$ at V_{OC} under AM 1.5G illumination. d) Mott Schottky plot at dark at 1 MHz of the pristine and Pre-TT D1 and D8 NF-OPVs.

Figure 7a shows a typical semicircle Cole–Cole plot for the fabricated pristine and Pre-TT based NF-OPVs at V_{OC} and their corresponding Bode plots presented in Figure S15a (Supporting Information), demonstrating the efficient transfer at the active layer/electrode interface.[96,97] We can see that all the analyzed NF-OPVs derived a single process illustrated by one arc attitude. First, regarding the types of devices, we observed that D8 devices exhibited smaller arc radius along with lower impedance than D1 devices. This might be attributed to the thickness optimization process performed to the D8 NF-OPVs, revealing their better performance. Second, regarding the Pre-TT approach, we noticed that both types of D1 and D8 showed smaller arc radii for the Pre-TT based devices than their corresponding pristine ones. This might consider the diminishing in the Pre-TT devices resistance,[33,96,97] matching their lower R_S obtained by the J–V characteristics (Table 1). Moreover, it was interesting to record the same behavior at short circuit voltage (0.0 V), near to the maximum power point voltage (V_{MPP} = 0.2 V) and at V_{MPP} of 0.5 V applied bias voltages as shown in Figure S15b–d (Supporting Information), respectively. Furthermore, the lower frequency arc decreases for the Pre-TT devices (D1-Pre-TT and D8- Pre-TT) which is the same behavior of arc size. We can interpret that the charge accumulation can be efficiently extracted through the contacts of the Pre-TT devices more than the pristine ones, as proposed by Arredondo et al.[99] This behavior confirms the effective contribution of the Pre-TT approach that improve the devices performance (Table 1), especially D8-Pre-TT as it possessed the lowest low-frequency arc which describes the less pronounced charge accumulation effect, correlating with the lowest leakage current (Figure 3a), lowest R_S, highest J_{SC} and as a sequence, reflecting their champion PCE. In contrast to the pristine devices, which have a higher low-frequency arc as well as higher leakage current (Figure 3a) and lower J_{SC} values, indicating their drop performance behavior (Table 1). Same behavior was observed in our previous reported work[33,100] as well as Upama et al.[23]

Another important consideration in short circuit conditions (Figure S15b, Supporting Information), as the Pre-TT based devices showed lower Z´ (real part-X axis) -Z´´ (imaginary part-Y axis) values than the pristine based ones. It indicates that the Pre-TT devices show rapid charge extraction, in contrast to the pristine ones, which contributes to the J_{SC} values of the devices which are highly consistent with the results of the J–V characteristics (listed in Table 1) and the previously discussed photo-physics measurements (Figure 4) as well as the performed optical analysis (Figure 3), revealing that the improvement of the J_{SC} of the Pre-TT devices has the main contribution to the PCE enhancement. To get more perception regarding the physical parameters of the fabricated NF-OPVs, we carried out an electrical equivalent circuit to fit the experimental Z'–Z''. The electrical component used to properly fit the plots (solid lines) is illustrated in the inset Figure 7a, the fitted parameters were summarized in Table S9 (Supporting Information). We used Debye model[101] equivalent circuit that consists of a parallel association of resistors (R) and capacitor (C) providing 3RC elements in series, where a distributed resistors (R) represent the resistance of electrons transportation in each layer where R_1, $R_{2,}$ and R_3 referring to PEDOT:PSS, PM6:Y7 and the PDINO layer, respectively. In addition, C refers to the geometrical capacitance values of each corresponding layer. R_S represents the series resistance from the ITO layer as well the ohmic contact resistance due to the interface between the ITO and the HTL in the conventional structure of the OPVs[96,97,102] and L is the added inductor to fit the data at high frequency.[96] Moreover, it is important to mention that the R_4C_4 elements were in series and attached in parallel to $R_3C_{3,}$ representing the PDINO interfacial layer as proposed by Debye model.[101]

Regarding the fitted data used to interpret the obtained results, it is worth to notice that the fitted capacitance values for each layer in the device were in an excellent agreement with the theoretical values (listed in Table S9, Supporting Information and calculated using Equation S4 and Tables S7 and S8, Supporting Information), indicating that the obtained Z'-Z'' data at V_{OC} were governed by the metal-insulator-metal model (MIM),[103] depicting the presence of fully depleted layers approach.[87,103] In addition, we observed that the C_4 values, representing the extra impeded traps in the PDINO layer, were reduced upon the Pre-TT step as listed in Table S9 (Supporting Information). It reveals that more trap defects were created in the PDINO layer in the pristine devices, hindering the charge carrier collection and transportation that in turn lowering their performance in contrary to the Pre-TT devices.[101,102]

Regarding the fitted resistance values listed in Table S9 (Supporting Information), it can be seen that the R_S value showed an insignificant increase for the Pre-TT devices more than the pristine ones. Moreover, as illustrated in Figure 7b, in both devices of $D1$ and $D8$, on one hand, we detected that the values of R_1 and R_3 representing the interfacial layers of PEDOT:PSS and PDINO layers, respectively, were declined upon applying the Pre-TT approach to the Pre-TT devices. Where R_1 values of $D1$ and $D8$ reduced from 17.0 to 15.6 Ω and 11.4 to 7.3 Ω, respectively, for the pristine and the Pre-TT cells, respectively. In the same way, R_3 values of $D1$ and $D8$ were decreased from 16.0 to 13.0 and 17.0 to 15.3, respectively, for the pristine and the Pre-TT devices, respectively. On the other hand, it was interesting to find that the values of R_2 representing the PM6:Y7 active layer did not show any difference upon the Pre-TT step for both D1 and D8 devices as shown in Figure 7b. Accordingly, the R_{total} values were more controlled by the resistance of the interfacial layers, that rather diminished from 37.9 to 35.2 Ω of the D1-W/O Pre-TT and D1- Pre-TT, respectively, and from 31.9 to 28.4 Ω for the D8-W/O Pre-TT and D8- Pre-TT, respectively, as displayed in Figure S16a (Supporting Information). Hence, the Pre-TT based cells showed a remarkable enhancement in suppressing the PEDOT:PSS and PDINO films resistance ($R1$ and $R3$), leading to an enhanced path of charge transportation and charge carriers collection, diminishing the recombination in the treated devices [88,96] as verified in the previous sections. In addition, we suggested that this enhancement in the interfaces between the blend and the interfacial layers might be attributed to the homogenous film morphology obtained for the Pre-TT films as observed by the AFM analysis in **Figure 8** (in the following discussion). It further explains their enhanced NF-OPVs

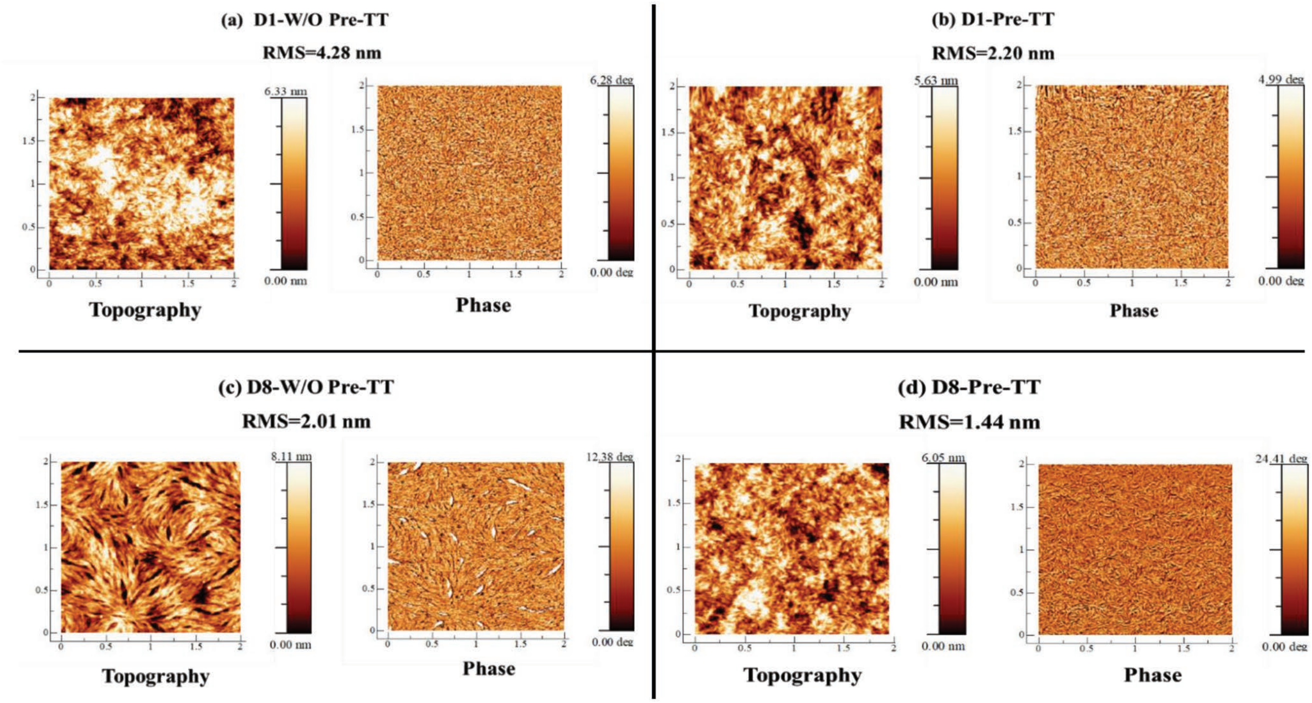

Figure 8. AFM topography and phase images of the PM6:Y7 blend films based on the fabricated devices a) D1-W/O Pre-TT, b) D1-Pre-TT, c) D8-W/O Pre-TT, and d) D8-Pre-TT.

performance obtained by the *J*–*V* characteristics under same illumination conditions (Table 1).

Furthermore, by analyzing the fitted data and estimating the total value of the extracted charge time (τ_{total}) for the fabricated devices listed in Table S9 (Supporting Information), we can see a significant diminish in the τ_{total} values for the Pre-TT cells than the pristine ones as illustrated in Figure S16b (Supporting Information), which endorse the CE and TPV behavior (Figure 4).

Upon these obtained results, we found that the Pre-TT approach contributed to reducing the impedance of the fabricated Pre-TT NF-OPVs, reflecting less implanted trap sites in the corresponding blend and interfaces within the layers of the treated devices, assisting charge transportation and collection, that highly matched with the calculated n_{id} (Figure 5b) and the E_{U} values (Figure 3c) observed for the Pre-TT devices. In addition, this behavior similarly followed the observed trend in the previous characteristics, endorsing the improvement effect upon applying the Pre-TT approach.

IS technique was performed in an alternative methodology, explaining the mechanisms behind the performance enhancement of the Pre-TT devices using the capacitance-frequency (C*f*) measurements to calculate the trap density of state (DOS) of the devices. It allows us to understand the electric properties of the fabricated devices, through investigating the interfacial charge transfer along with carrier recombination mechanisms.[104] It is well known that as the trap densities are high, then trapped charge carrier still can participate in the transportation by thermally hopping or tunneling (shallow traps), while deep traps creates recombination centers due to hardly excited back charges.[24] This characterization has been performed for OPVs in many research work to obtain the change in trap emission and disorder-induced tail states within the devices.[24,96,104–106] Consequently, the traps DOS at a given energy level, E_ω, can be determined by varying the capacitance of the device with frequency. This reveals the trapping and the charge release by shallow traps in the band gap near to the Fermi energy level as proposed in Equation (3) [24,106]

$$\text{DOS}(E_\omega)_{\text{traps}} = -\frac{V_{\text{OC}}\omega}{tq\,T\,k_{\text{B}}}\frac{\partial C}{\partial \omega} \tag{3}$$

where C is the measured capacitance, V_{OC} is the open circuit voltage obtained by the *J*–*V* characteristics (Table 1), ω is the angular frequency, t is the layer thickness, k_{B} is the Boltzmann constant, q is the electron charge and T is room temperature (300 K). Then, the following Equation (4) considers the relation of the trap-DOS as function of energy dependent

$$(E_\omega)_{\text{traps}} = k_{\text{B}}\,T\ln\frac{2\beta N}{\omega} = E_{\text{O}} - k_{\text{B}}T\ln\omega \tag{4}$$

where β is the cross-section and N is the effective density of state.[107] Assuming $2\beta N$ as an independent of the frequency value, hence, the change in its value is correlated to the shift in the DOS values as a function of energy (E_{O})[102] which is explicitly explained in the Supporting Information.

Figure 7c displays the plot of the calculated trap-DOS as a function of energy for the fabricated devices. It describes a single exponential trap distribution for all devices, revealing the same trap activation energy and carrier response.[108] However, a bit higher DOS values were observed for D1 and D8 Pre-TT devices represented in the shift of E_{O} value, as explained by Equation (4), calculating the values of the energy shifting (X) for the pristine cells (see Equation S5, Supporting Information), presented by the solid lines in Figure S17 (Supporting Information). Where, the Pre-TT devices demonstrated higher energy by one order of magnitude than the pristine ones, reflecting less localized interfacial induced defects compared to the pristine devices.[24,102,107,109,110] This behavior was interestingly matched with the suppressing of recombination behavior in Figure 5 which explains the higher J_{SC} obtained for the treated devices through the Pre-TT approach.

Furthermore, in Equation (4), the slope of the tail given by $k_{\text{B}}T$ measures the extent of the distribution of localized states; in other words, it is an indirect measure of the disorder in the semiconductor.[111] Depending on their relative energetic position from the band edge, trap depth can be determined. Few $k_{\text{B}}T$ from the band edge represents the shallow traps and several kT reveal the deep traps that lie further.[56] In Figure 7c, we depicted that the tail of localized state was a bit reduced for the Pre-TT as compared to the pristine ones. This behavior indicates that the pristine based devices possess deeper traps in the tail state HOMO. Such deep states act as recombination centers for charge carriers, resulting in reducing their overall lifetime and in turn devices performance.[24] Interestingly, this behavior is consistent with the E_{U} values aforementioned in Figure 3c.

To get further insight into the influence of the Pre-TT approach on the fabricated devices, we used the IS to investigate the dark and light intensity-dependent capacitance–voltage (*C*–*V*) characteristics. First, Figure 7d explains the Mott-Schottky of *C*–*V* data measured in the dark at the applied frequency of 1 MHz for NF-OPVs with pristine and Pre-TT devices. Two regions have been recorded from the entire samples, the linear region 1 from 0.0 to 1.0 V, corresponding to the contribution from the PM6 donor phase and region 2 from 0.0 V to 1.0 V that attributed to the Y7 acceptor phase[106,112] as demonstrated in the inset of Figure 7d. We observed that the slope of the curves in region 2 is almost the same, while region 1 has shown different slopes, indicating various traps contribution in each device.[106] Accordingly, from region 1, we evaluated the built-in voltage (V_{bi}), by finding the plot intercept with the *x*-axis as demonstrated in Figure 7d. The values of V_{bi} were 0.89 V, 0.93 V, 0.87 V, and 0.98 V for D1-W/O Pre-TT, D1-Pre-TT, D8-W/O Pre-TT, and D8-Pre-TT, respectively. It was interesting to find that the Pre-TT devices possessed higher V_{bi} values than their corresponding pristine NF-OPVs. The enhanced V_{bi} assists the collection of holes and repels electrons at the interfaces, reducing the interfacial recombination, and thereby enhancing the device performance[88] as presented by our Pre-TT devices. Therefore, the low V_{bi} values signify that the photovoltaic devices work inefficiently through impeding the charge carriers extraction instead of assisting it,[23,33] confirming the lower performance obtained by the pristine devices. As a sequence, these results demonstrated that the Pre-TT approach not only reduced the trapes states in the blend films, but also improves the interfaces charge transport, leading to overall improvement in the device performance. Moreover, it is worth to mention that the

Pre-TT devices showed a higher chemical capacitance than the pristine ones (Figure 7d), resulting in less localized stated in the bandgap that leads to diminishing the carrier recombination.[23,96] Second, for further investigation regarding these observed traps sites for the fabricated NF-OPVs, we followed the standard Mott-Schottky analysis to calculate the charge carrier density (N_{PM6}) in region 1 using Equation (5) [87,106,112]

$$\left(\frac{A}{C}\right)^2 = \frac{2(V - V_{Bi})}{q\varepsilon_O \varepsilon_{PM6} N_{PM6}} \tag{5}$$

where A is the active area of the device, C is the capacitance, V is the applied voltage, V_{Bi} is the built-in voltage, q is the elementary charge, ε_O is the vacuum permittivity, ε_{PM6} is the relative dielectric constant of PM6 donor polymer.

Under the assumption of $N_{Y7} >> N_{PM6}$ which has been calculated and explained in Figure S18a (Supporting Information), then applying Equation (5) to the $C–V$ measurements at 1 MHz under different illumination intensities (P_{light}) for pristine and Pre-TT devices, we obtained the N_{PM6} versus the P_{light} illustrated in Figure S18b (Supporting Information). It can be seen that the charge carrier concentration increased upon light intensities for the entire devices as predicted phenomena of charge photogeneration in the bulk.[24] However, on one hand, it was interesting to detect that the slopes of D1-W/O Pre-TT and D8-W/O Pre-TT were increased more sharply than the slopes of D1-Pre-TT and D8-Pre-TT cells. This attitude for the pristine devices might be ascribed to significant located trap states into the bulk [24,106,113] which correlate with the measurements of the DOS in Figure 7c. On the other hand, the slope of the D1-PreTT and D8-Pre-TT devices were steadier upon the effect of the light intensities which reflects the less contribution regarding traps.[24] Accordingly, the Pre-TT approach provides less recombination behavior which leads to higher charge carrier concentration (Figure S18b, Supporting Information) that reflects the extraordinary J_{SC} obtained from Pre-TT based devices that is greatly matching the CE and TPV characteristics (Figure 5).

2.5. Morphology

A microscopic view characteristic was performed through atomic force microscope (AFM) to investigate the active blend morphology variation upon the effect of Pre-TT approach. We carried out the morphological characterization of the PM6:Y7 blend films over the PEDOT:PSS layer, considering same conditions of the pristine (W/O Pre-TT) as well as the Pre-TT based devices of D1 and the optimized D8, as the Pre-TT approach combines the treatment of both PEDOT:PSS along with the active blend PM6:Y7 film as explained in Figure S1 (Supporting Information) at the Experimental section. Figure 8 displays the AFM topography images and the corresponding phases of the blend films of the mentioned based devices. We can notice that the root mean square surface roughness (RMS) values of the Pre-TT blend films were lower than the pristine ones. Where the RMS of the pristine blend film of D1-W/O Pre-TT is 4.28 nm (Figure 8a) which is doubled the RMS of the D1-Pre-TT film (2.20 nm—Figure 8b).

Moreover, the same behavior was obtained for the pristine blend film of D8-W/O Pre-TT with RMS of 2.01 nm (Figure 8c), which is as well higher than the D8-Pre-TT film of RMS = 1.44 nm—as shown in Figure 8d. First, regarding the blend thickness, the surface roughness and the size of the domain increase as the thickness of the PM6:Y7 film increases[30] as shown in D1 (150 nm), in contrast to the optimized D8 (100 nm) that presented less PM6:Y7 film roughness in both cases of pristine and Pre-TT based films. Second, regarding the Pre-TT approach, it is noticeable that the surface roughness and the phase features of Pre-TT films were different than the pristine films for both of D1 and D8, where the diminishing in the RMS values of the Pre-TT films, providing smoother surface, might be ascribed to the decline in the size of the domains.[30] As already reported by Zhang et al. and Guo et al.,[114,115] temperature causes a pre-aggregation of the PM6 already in the solution, resulting in smaller PM6 fibrillar domain size, which affects the miscibility and crystallinity of non-fullerene acceptors resulting in a better nanoscale phase separation.[116,117] Furthermore, the field emission-scanning electron microscope images displayed in Figure S19 (Supporting Information) were conducted for the pristine and Pre-TT D8 based films (PEDOT:PSS/PM6:Y7). It demonstrates that the pristine based films showed the strongest aggregation, in contrast to the Pre-TT based films that exhibited more fine, uniform, and compact film morphology. Consequently, despite the simplicity of the Pre-TT step, but it presents obvious effect on the morphology of the treated films that led to a remarkably smooth surface (lower values of RMS) and enhanced phase order separation features with better dispersity.[19] Since the small domain sizes assist the excitons in the active layer blend to reach the donor/acceptor interface, and in turn dissociate into free carriers.[30] Hence, it is worth to mention that this enhanced morphology of the Pre-TT based films might reflect the enhancement of their based film absorption (Figure 3b), J_{SC} of their based devices (Figure 2a and Table 1) as well as manifesting the lowest R_S and leakage current[23,33] (Figure 3), resulting in improving their PCE. Furthermore, this observation supports the IS characteristics in Figure 7a, where the pristine devices possessed the highest low-frequency arc that describes more pronounced charge accumulation effect that could be originated from the pristine morphology disorder of the blend, providing lower overall performance. In contrast to the Pre-TT devices, as it exhibited less traps contribution as confirmed by the closest n_{id} to 1, lowest E_U values, highest P_{diss} along with the optical and the previously discussed electrical IS characteristics, which might be emanated from the fine-tuning of their based film morphology upon the Pre-TT approach. Thus, the Pre-TT approach provides a morphological control, which is beneficial for tuning the film surface morphology that greatly enhances the overall performance of the device.

3. Conclusion

In summary, aiming to enhance the photovoltaic performance, we explicitly conducted a systematic investigation regarding the influence of the Pre-TT approach on the performance of the NF-OPVs. Applying the Pre-TT step critically affects the PEDOT:PSS/PM6:Y7 blend morphologies and thus the overall performance of the devices. Interestingly, this paper puts the spotlight on the extraordinary J_{SC} values obtained by the Pre-TT devices, where the optimized treated devices of D8-Pre-TT exhibited a pioneer enhanced J_{SC} value of 32.65 mA cm^{-2} along with improved PCE of 17.92. We observed that the treated based films exhibited smoother surface roughness, revealing their lower R_S, and lower leakage current, which leads to high carrier transport and suppressed charge carrier recombination in the resulting NF-OPVs. Indispensably, a critical challenge for the current NFA-based OPVs is to avoid the strong phase separation upon blending and deposition, which applied through the Pre-TT approach, leading to the balanced hole and electron mobility along with low non-geminate recombination that might be the key parameter leading to the remarkable enhancement observed in the performance of the Pre-TT NF-OPVs. Moreover, the enhanced J_{SC} values noticed for the Pre-TT devices were mainly due to their high EQE values and high P_{diss} than the corresponding pristine NF-OPVs, correlating their remarkable PL quench of the Pre-TT films, reflecting the efficient charge transfer at the PEDOT:PSS/PM6:Y7 interfaces Furthermore, the IS characteristics were conducted through investigating the Nyquist plot, Cf-DOS calculations and the C–V characteristics, providing an efficient insight study that accurately detected the recombination contribution that was more obvious for the pristine devices which disclose their lower performance. Accordingly, the Pre-TT approach diminishes the traps and enhances the interface charge transfer through enhancing the carrier dynamics of the treated devices, triggering a promising approach for boosting the J_{SC} along with the photovoltaic performance of the treated devices.

Supporting Information

Supporting Information is available from the Wiley Online Library or from the author.

Acknowledgements

E.M. acknowledges the Agency for Management of University and Research Grants (AGAUR) for receiving the fund with grant number 2019 FI_B01102. ICIQ and ICREA are also acknowledged for the contribution of the photoluminescence and advanced optoelectronic measurements as well as the discussion of the results. This work was further supported by the Spanish Ministerio de Ciencia, Innovación PDI2021-128342OB-I00. The authors further acknowledge the Diptació de Tarragona 2021CM14.

Conflict of Interest

The authors declare no conflict of interest.

Data Availability Statement

The data that support the findings of this study are available from the corresponding author upon reasonable request.

Keywords

balanced electron/hole mobility, binary heterojunctions, interface morphology, nonfullerene organic photovoltaics, thermal annealing

Received: September 25, 2022
Revised: November 22, 2022

---

[1] Y. Li, Y. Guo, Z. Chen, L. Zhan, L. Zuo, C. He, Z. Bi, N. Yao, S. Li, G. Zhou, Y. Yi, Y. M. Yang, H. Zhu, W. Ma, F. Gao, F. Zhang, H. Chen, *Energy Environ. Sci.* **2022**, *15*, 855.
[2] Q. Liu, Y. Jiang, K. Jin, J. Qin, J. Xu, W. Li, J. Xiong, J. Liu, Z. Xiao, K. Sun, S. Yang, X. Zhang, L. Ding, *Sci. Bull.* **2020**, *65*, 272.
[3] Y. Lin, B. Adilbekova, Y. Firdaus, E. Yengel, H. Faber, M. Sajjad, X. Zheng, E. Yarali, A. Seitkhan, O. M. Bakr, A. El-Labban, U. Schwingenschlögl, V. Tung, I. McCulloch, F. Laquai, T. D. Anthopoulos, *Adv. Mater.* **2019**, *31*, 1902965.
[4] Y. Cui, H. Yao, J. Zhang, T. Zhang, Y. Wang, L. Hong, K. Xian, B. Xu, S. Zhang, J. Peng, Z. Wei, F. Gao, J. Hou, *Nat. Commun.* **2019**, *10*, 2515.
[5] Y. Cui, H. Yao, L. Hong, T. Zhang, Y. Tang, B. Lin, K. Xian, B. Gao, C. An, P. Bi, W. Ma, J. Hou, *Natl. Sci. Rev.* **2020**, *7*, 1239.
[6] J. Lee, D. H. Sin, B. Moon, J. Shin, H. G. Kim, M. Kim, K. Cho, *Energy Environ. Sci.* **2017**, *10*, 247.
[7] M. Riede, D. Spoltore, K. Leo, *Adv. Energy Mater.* **2021**, *11*, 2002653.
[8] W. Zhao, D. Qian, S. Zhang, S. Li, O. Inganäs, F. Gao, J. Hou, *Adv. Mater.* **2016**, *28*, 4734.
[9] A. Armin, W. Li, O. J. Sandberg, Z. Xiao, L. Ding, J. Nelson, D. Neher, K. Vandewal, S. Shoaee, T. Wang, H. Ade, T. Heumüller, C. Brabec, P. Meredith, *Adv. Energy Mater.* **2021**, *11*, 2003570.
[10] B. Kan, J. Zhang, F. Liu, X. Wan, C. Li, X. Ke, Y. Wang, H. Feng, Y. Zhang, G. Long, R. H. Friend, A. A. Bakulin, Y. Chen, *Adv. Mater.* **2018**, *30*, 1704904.
[11] S. Liu, J. Yuan, W. Deng, M. Luo, Y. Xie, Q. Liang, Y. Zou, Z. He, H. Wu, Y. Cao, *Nat. Photonics* **2020**, *14*, 300.
[12] D. Qian, Z. Zheng, H. Yao, W. Tress, T. R. Hopper, S. Chen, S. Li, J. Liu, S. Chen, J. Zhang, X. K. Liu, B. Gao, L. Ouyang, Y. Jin, G. Pozina, I. A. Buyanova, W. M. Chen, O. Inganäs, V. Coropceanu, J. L. Bredas, H. Yan, J. Hou, F. Zhang, A. A. Bakulin, F. Gao, *Nat. Mater.* **2018**, *17*, 703.
[13] P. Sonar, J. P. F. Lim, K. L. Chan, *Energy Environ. Sci.* **2011**, *4*, 1558.
[14] W. Liu, X. Xu, J. Yuan, M. Leclerc, Y. Zou, Y. Li, *ACS Energy Lett.* **2021**, *6*, 598.
[15] N. A. Ran, S. Roland, J. A. Love, V. Savikhin, C. J. Takacs, Y. T. Fu, H. Li, V. Coropceanu, X. Liu, J. L. Brédas, G. C. Bazan, M. F. Toney, Di. Neher, T. Q. Nguyen, *Nat. Commun.* **2017**, *8*, 1.
[16] H. Kang, W. Lee, J. Oh, T. Kim, C. Lee, B. J. Kim, *Acc. Chem. Res.* **2016**, *49*, 2424.
[17] J. Liu, S. Chen, D. Qian, B. Gautam, G. Yang, J. Zhao, J. Bergqvist, F. Zhang, W. Ma, H. Ade, O. Inganäs, K. Gundogdu, F. Gao, H. Yan, *Nat. Energy* **2016**, *1*, 16089.
[18] D. Baran, T. Kirchartz, S. Wheeler, S. Dimitrov, M. Abdelsamie, J. Gorman, R. S. Ashraf, S. Holliday, A. Wadsworth, N. Gasparini, P. Kaienburg, H. Yan, A. Amassian, C. J. Brabec, J. R. Durrant, I. McCulloch, *Energy Environ. Sci.* **2016**, *9*, 3783.
[19] J. Yuan, Y. Zhang, L. Zhou, G. Zhang, H. L. Yip, T. K. Lau, X. Lu, C. Zhu, H. Peng, P. A. Johnson, M. Leclerc, Y. Cao, J. Ulanski, Y. Li, Y. Zou, *Joule* **2019**, *3*, 1140.
[20] Y. Cui, H. Yao, J. Zhang, K. Xian, T. Zhang, L. Hong, Y. Wang, Y. Xu, K. Ma, C. An, C. He, Z. Wei, F. Gao, J. Hou, *Adv. Mater.* **2020**, *32*, 1908205.

[21] J. Lv, H. Tang, J. Huang, C. Yan, K. Liu, Q. Yang, D. Hu, R. Singh, J. Lee, S. Lu, G. Li, Z. Kan, *Energy Environ. Sci.* **2021**, *14*, 3044.
[22] G. Zhang, K. Zhang, Q. Yin, X. F. Jiang, Z. Wang, J. Xin, W. Ma, H. Yan, F. Huang, Y. Cao, *J. Am. Chem. Soc.* **2017**, *139*, 2387.
[23] M. B. Upama, N. K. Elumalai, M. A. Mahmud, M. Wright, D. Wang, C. Xu, A. Uddin, *Sol. Energy Mater. Sol. Cells* **2018**, *176*, 109.
[24] H. F. Haneef, A. M. Zeidell, O. D. Jurchescu, *J. Mater. Chem. C* **2020**, *8*, 759.
[25] N. Gasparini, M. Salvador, S. Strohm, T. Heumueller, I. Levchuk, A. Wadsworth, J. H. Bannock, J. C. de Mello, H. J. Egelhaaf, D. Baran, I. McCulloch, C. J. Brabec, *Adv. Energy Mater.* **2017**, *7*, 1700770.
[26] K. A. O'Hara, D. P. Ostrowski, U. Koldemir, C. J. Takacs, S. E. Shaheen, A. Sellinger, M. L. Chabinyc, *ACS Appl. Mater. Interfaces* **2017**, *9*, 19021.
[27] K. Weng, L. Ye, L. Zhu, J. Xu, J. Zhou, X. Feng, G. Lu, S. Tan, F. Liu, Y. Sun, *Nat. Commun.* **2020**, *11*, 2855.
[28] K. Fukuda, K. Yu, T. Someya, *Adv. Energy Mater.* **2020**, *10*, 2000765.
[29] F. Zhao, C. Wang, X. Zhan, *Adv. Energy Mater.* **2018**, *8*, 1703147.
[30] S. Gu, H. Neugebauer, N. S. Sariciftci, *Chem. Rev.* **2007**, *107*, 1324.
[31] B. Du, R. Geng, W. Tan, Y. Mao, D. Li, X. Zhang, D. Liu, W. Tang, W. Huang, T. Wang, *J. Energy Chem.* **2021**, *54*, 131.
[32] F. Jin, G. Ding, Y. Wang, J. Yuan, W. Guo, H. Yuan, C. Sheng, W. Ma, H. Zhao, *J. Phys. Chem. C* **2017**, *121*, 8804.
[33] E. Moustafa, A. A. A. Torimtubun, J. Pallarès, L. F. Marsal, *Sol. RRL* **2021**, *6*, 2100480.
[34] Y. Li, M. Wang, Q. Zhang, Z. Wu, H. Lim, Y. Wang, H. Qin, J. Yang, C. Gao, H. Young Woo, J. Yuan, *Chem. Eng. J.* **2022**, *428*, 131232.
[35] X. Li, W. Zhang, K. Usman, J. Fang, *Adv. Energy Mater.* **2018**, *8*, 1702730.
[36] J. Wu, J. Lee, Y. C. Chin, H. Yao, H. Cha, J. Luke, J. Hou, J. S. Kim, J. R. Durrant, *Energy Environ. Sci.* **2020**, *13*, 2422.
[37] J. Yao, B. Qiu, Z. G. Zhang, L. Xue, R. Wang, C. Zhang, S. Chen, Q. Zhou, C. Sun, C. Yang, M. Xiao, L. Meng, Y. Li, *Nat. Commun.* **2020**, *11*, 2726.
[38] A. M. Peiro, P. Ravirajan, K. Govender, D. S. Boyle, P. O'Brien, D. D. C. Bradley, J. Nelson, J. R. Durrant, *J. Mater. Chem.* **2006**, *16*, 2088.
[39] X. Wang, L. Zhang, L. Hu, Z. Xie, H. Mao, L. Tan, Y. Zhang, Y. Chen, *Adv. Funct. Mater.* **2021**, *31*, 2102291.
[40] M. B. Upama, M. A. Mahmud, G. Conibeer, A. Uddin, *Sol. RRL* **2020**, *4*, 2000241.
[41] L. Zhan, S. Li, T. K. Lau, Y. Cui, X. Lu, M. Shi, C. Z. Li, H. Li, J. Hou, H. Chen, *Energy Environ. Sci.* **2020**, *13*, 635.
[42] P. Schilinsky, C. Waldauf, J. Hauch, C. J. Brabec, *J. Appl. Phys.* **2004**, *95*, 2816.
[43] B. Qi, J. Wang, *Phys. Chem. Chem. Phys.* **2013**, *15*, 8972.
[44] N. Grossiord, J. M. Kroon, R. Andriessen, P. W. M. Blom, *Org. Electron.* **2012**, *13*, 432.
[45] C. M. Proctor, T. Q. Nguyen, *Appl. Phys. Lett.* **2015**, *106*, 083301.
[46] G. A. H. Wetzelaer, M. Kuik, M. Lenes, P. W. M. Blom, *Appl. Phys. Lett.* **2011**, *99*, 153506.
[47] A. Armin, I. Kassal, P. E. Shaw, M. Hambsch, M. Stolterfoht, D. M. Lyons, J. Li, Z. Shi, P. L. Burn, P. Meredith, *J. Am. Chem. Soc.* **2014**, *136*, 11465.
[48] A. Armin, M. Velusamy, P. Wolfer, Y. Zhang, P. L. Burn, P. Meredith, A. Pivrikas, *ACS Photonics* **2014**, *1*, 173.
[49] H. Tang, H. Chen, C. Yan, J. Huang, P. W. K. Fong, J. Lv, D. Hu, R. Singh, M. Kumar, Z. Xiao, Z. Kan, S. Lu, G. Li, *Adv. Energy Mater.* **2020**, *10*, 2001076.
[50] S. R. Forrest, *MRS Bull.* **2005**, *30*, 28.
[51] F. Urbach, *Phys. Rev.* **1953**, *92*, 1324.
[52] N. Jain, N. Chandrasekaran, A. Sadhanala, R. H. Friend, C. R. McNeill, D. Kabra, *J. Mater. Chem. A* **2017**, *5*, 24749.
[53] Z. He, B. Xiao, F. Liu, H. Wu, Y. Yang, S. Xiao, C. Wang, T. P. Russell, Y. Cao, *Nat. Photonics* **2015**, *9*, 174.
[54] F. Wang, M. Yang, Y. Zhang, L. Yang, L. Fan, S. Lv, X. Liu, D. Han, J. Yang, *Adv. Sci.* **2019**, *6*, 1801170.
[55] C. H. Peters, I. T. Sachs-Quintana, W. R. Mateker, T. Heumueller, J. Rivnay, R. Noriega, Z. M. Beiley, E. T. Hoke, A. Salleo, M. D. McGehee, *Adv. Mater.* **2012**, *24*, 663.
[56] C. Kaiser, O. J. Sandberg, N. Zarrabi, W. Li, P. Meredith, A. Armin, *Nat. Commun.* **2021**, *12*, 3988.
[57] D. E. Markov, E. Amsterdam, P. W. M. Blom, A. B. Sieval, J. C. Hummelen, in *Organic Optoelectronics and Photonics*, Vol. *5464* (Eds.: P. L. Heremans, M. Muccini, H. Hofstraat), SPIE - INT SOC Optical Engineering, Bellingham **2004**, p. 449.
[58] G. Xing, N. Mathews, S. Sun, S. S. Lim, Y. M. Lam, M. Graẗzel, S. Mhaisalkar, T. C. Sum, *Science* **2013**, *342*, 344.
[59] M. M. Emilio Palomares1, N. F. Montcada, W. Y., G. B. Jesus Jiménez Lopez, *Micro and Nano Technologies*, Elsevier, **2020**, pp. 49–79.
[60] A. Pockett, H. K. H. Lee, B. L. Coles, W. C. Tsoi, M. J. Carnie, *Nanoscale* **2019**, *11*, 10872.
[61] T. Liu, Z. Luo, Q. Fan, G. Zhang, L. Zhang, W. Gao, X. Guo, W. Ma, M. Zhang, C. Yang, Y. Li, H. Yan, *Energy Environ. Sci.* **2018**, *11*, 3275.
[62] N. K. Elumalai, A. Uddin, *Energy Environ. Sci.* **2016**, *9*, 391.
[63] I. Gelmetti, N. F. Montcada, A. Pérez-Rodríguez, E. Barrena, C. Ocal, I. García-Benito, A. Molina-Ontoria, N. Martín, A. Vidal-Ferran, E. Palomares, *Energy Environ. Sci.* **2019**, *12*, 1309.
[64] G. Garcia-Belmonte, P. P. Boix, J. Bisquert, M. Sessolo, H. J. Bolink, *Sol. Energy Mater. Sol. Cells* **2010**, *94*, 366.
[65] S. R. Cowan, A. Roy, A. J. Heeger, *Phys. Rev. B: Condens. Matter Mater. Phys.* **2010**, *82*, 245207.
[66] F. Zhao, S. Dai, Y. Wu, Q. Zhang, J. Wang, L. Jiang, Q. Ling, Z. Wei, W. Ma, W. You, C. Wang, X. Zhan, *Adv. Mater.* **2017**, *29*, 1700144.
[67] Z. Liu, N. Wang, *J. Mater. Chem. C* **2019**, *7*, 10039.
[68] P. Hartnagel, T. Kirchartz, *Adv. Theory Simul.* **2020**, *3*, 2000116.
[69] J. M. Foster, J. Kirkpatrick, G. Richardson, *J. Appl. Phys.* **2013**, *114*, 104501.
[70] G. Juka, K. Arlauskas, *Sol. Energy* **2010**, *38*, 1941.
[71] E. L. Meyer, *Int. J. Photoenergy* **2017**, *2017*, 8479487.
[72] V. Gupta, A. K. K. Kyaw, D. H. Wang, S. Chand, G. C. Bazan, A. J. Heeger, *Sci. Rep.* **2013**, *3*, 6.
[73] M. H. Jao, H. C. Liao, W. F. Su, *J. Mater. Chem. A* **2016**, *4*, 5784.
[74] K. Tvingstedt, C. Deibel, *Adv. Energy Mater.* **2016**, *6*, 1502230.
[75] Y. Tang, H. Sun, Z. Wu, Y. Zhang, G. Zhang, M. Su, X. Zhou, X. Wu, W. Sun, X. Zhang, B. Liu, W. Chen, Q. Liao, H. Y. Woo, X. Guo, *Adv. Sci.* **2019**, *6*, 1901773.
[76] V. D. Mihailetchi, L. J. A. Koster, P. W. M. Blom, C. Melzer, B. De Boer, J. K. J. Van Duren, R. A. J. Janssen, *Adv. Funct. Mater.* **2005**, *15*, 795.
[77] V. D. Mihailetchi, L. J. A. Koster, J. C. Hummelen, P. W. M. Blom, *Phys. Rev. Lett.* **2004**, *93*, 19.
[78] J.-L. Wu, F.-C. Chen, Y.-S. Hsiao, F.-C. Chien, P. Chen, C.-H. Kuo, M. H. Huang, C.-S. Hsu, *ACS Nano* **2011**, *5*, 959.
[79] B. H. Jiang, Y. P. Wang, C. Y. Liao, Y. M. Chang, Y. W. Su, R. J. Jeng, C. P. Chen, *ACS Appl. Mater. Interfaces* **2021**, *13*, 1076.
[80] J. Zhao, Y. Li, H. Lin, Y. Liu, K. Jiang, C. Mu, T. Ma, J. Y. Lin Lai, H. Hu, D. Yu, H. Yan, *Energy Environ Sci* **2015**, *8*, 520.
[81] J. A. Röhr, D. Moia, S. A. Haque, T. Kirchartz, J. Nelson, *J. Phys.: Condens. Matter* **2018**, *30*, 105901.
[82] S. A. Moiz, I. A. Khan, W. A. Younis, K. S. Karimov, in *Conducting Polymers* (Ed.: F. Yilmaz), IntechOpen, London **2016**, pp. 91–117.
[83] L. Ma, S. Zhang, H. Yao, Y. Xu, J. Wang, Y. Zu, J. Hou, *ACS Appl. Mater. Interfaces* **2020**, *12*, 18777.
[84] H. Choi, J. Lee, C. M. Oh, S. Jang, H. Kim, M. S. Jeong, S. H. Park, I. W. Hwang, *J. Mater. Chem. A* **2019**, *7*, 8805.
[85] H. Bristow, K. J. Thorley, A. J. P. White, A. Wadsworth, M. Babics, Z. Hamid, W. Zhang, A. F. Paterson, J. Kosco, J. Panidi, T. D. Anthopoulos, I. McCulloch, *Adv. Electron. Mater.* **2019**, *5*, 1900344.

[86] N. A. Mica, S. A. J. Thomson, I. D. W. Samuel, *Org. Electron.* **2018**, *63*, 415.
[87] N. Tokmoldin, S. M. Hosseini, M. Raoufi, L. Q. Phuong, O. J. Sandberg, H. Guan, Y. Zou, D. Neher, S. Shoaee, *J. Mater. Chem. A* **2020**, *8*, 7854.
[88] F. Wang, M. Yang, Y. Zhang, J. Du, S. Yang, L. Yang, L. Fan, Y. Sui, Y. Sun, J. Yang, *Nano Res.* **2021**, *14*, 2783.
[89] B. Lin, X. Zhou, H. Zhao, J. Yuan, K. Zhou, K. Chen, H. Wu, R. Guo, M. A. Scheel, A. Chumakov, S. V. Roth, Y. Mao, L. Wang, Z. Tang, P. Müller-Buschbaum, W. Ma, *Energy Environ. Sci.* **2020**, *13*, 2467.
[90] Y. Firdaus, V. M. Le Corre, J. I. Khan, Z. Kan, F. Laquai, P. M. Beaujuge, T. D. Anthopoulos, *Adv. Sci.* **2019**, *6*, 1802028.
[91] T. Mikie, A. Saeki, H. Masuda, N. Ikuma, K. Kokubo, S. Seki, *J. Mater. Chem. A* **2014**, *3*, 1152.
[92] K. Jiang, J. Zhang, Z. Peng, F. Lin, S. Wu, Z. Li, Y. Chen, H. Yan, H. Ade, Z. Zhu, A. K. Y. Jen, *Nat. Commun.* **2021**, *12*, 468.
[93] L. Zhang, X. Xu, B. Lin, H. Zhao, T. Li, J. Xin, Z. Bi, G. Qiu, S. Guo, K. Zhou, X. Zhan, W. Ma, *Adv. Mater.* **2018**, *30*, 1805041.
[94] S. Athanasopoulos, F. Schauer, V. Nádaždy, M. Weiß, F. J. Kahle, U. Scherf, H. Bässler, A. Köhler, *Adv. Energy Mater.* **2019**, *9*, 1900814.
[95] S. Wilken, O. J. Sandberg, D. Scheunemann, R. Österbacka, *Sol. RRL* **2020**, *4*, 1900505.
[96] E. Von Hauff, *J. Phys. Chem. C* **2019**, *123*, 11329.
[97] E. Osorio, J. G. Sánchez, L. N. Acquaroli, M. Pacio, J. Ferré-Borrull, J. Pallarès, L. F. Marsal, *ACS Omega* **2017**, *2*, 3091.
[98] L. Contreras-Bernal, S. Ramos-Terrón, A. Riquelme, P. P. Boix, J. Idígoras, I. Mora-Seró, J. A. Anta, *J. Mater. Chem. A* **2019**, *7*, 12191.
[99] B. Arredondo, M. B. Martín-López, B. Romero, R. Vergaz, P. Romero-Gomez, J. Martorell, *Sol. Energy Mater. Sol. Cells* **2016**, *144*, 422.
[100] E. Moustafa, M. Méndez, J. Pallarès, L. F. Marsal, *Sol. Energy Mater. Sol. Cells* **2022**, *248*, 111985.
[101] Z. He, K. Huang, C. Guo, Z. Jin, C. Hou, *AIP Adv.* **2019**, *9*, 045321.
[102] E. Moustafa, J. G. Sánchez, L. F. Marsal, J. Pallarès, *ACS Appl. Energy Mater.* **2021**, *4*, 4099.
[103] H. Schroeder, *J. Appl. Phys.* **2015**, *117*, 215103.
[104] S. S. Hegedus, E. A. Fagen, *J. Appl. Phys.* **1992**, *71*, 5941.
[105] S. Wang, P. Kaienburg, B. Klingebiel, D. Schillings, T. Kirchartz, *J. Phys. Chem. C* **2018**, *122*, 9795.
[106] B. Ecker, J. C. Nolasco, J. Pallarés, L. F. Marsal, J. Posdorfer, J. Parisi, E. Von Hauff, *Adv. Funct. Mater.* **2011**, *21*, 2705.
[107] T. Walter, R. Herberholz, C. Müller, H. W. Schock, *J. Appl. Phys.* **1996**, *80*, 4411.
[108] G. Garcia-Belmonte, A. Munar, E. M. Barea, J. Bisquert, I. Ugarte, R. Pacios, *Org. Electron.* **2008**, *9*, 847.
[109] J. Bhattacharya, P. H. Joshi, R. Biswas, V. L. Dalal, *Sol. Energy Mater. Sol. Cells* **2017**, *164*, 70.
[110] J. Wu, J. Luke, H. K. H. Lee, P. Shakya Tuladhar, H. Cha, S. Y. Jang, W. C. Tsoi, M. Heeney, H. Kang, K. Lee, T. Kirchartz, J. S. Kim, J. R. Durrant, *Nat. Commun.* **2019**, *10*, 5159.
[111] Z. Chen, T. Wang, Z. Wen, P. Lu, W. Qin, H. Yin, X. Hao, *ACS Energy Lett.* **2021**, *6*, 3203.
[112] J. C. Nolasco, A. Sánchez-Díaz, R. Cabŕ, J. Ferŕ-Borrull, L. F. Marsal, E. Palomares, J. Pallar̀s, *Appl. Phys. Lett.* **2010**, *97*, 013305.
[113] A. Seemann, H. J. Egelhaaf, C. J. Brabec, J. A. Hauch, *Org. Electron.* **2009**, *10*, 1424.
[114] H. Zhang, H. Yao, J. Hou, J. Zhu, J. Zhang, W. Li, R. Yu, B. Gao, S. Zhang, J. Hou, *Adv. Mater.* **2018**, *30*, 1800613.
[115] C. Guo, D. Li, L. Wang, B. Du, Z. X. Liu, Z. Shen, P. Wang, X. Zhang, J. Cai, S. Cheng, C. Yu, H. Wang, D. Liu, C. Z. Li, T. Wang, *Adv. Energy Mater.* **2021**, *11*, 2102000.
[116] T. Wang, J. L. Bredas, *J. Am. Chem. Soc.* **2021**, *143*, 1822.
[117] M. Gao, W. Wang, J. Hou, L. Ye, *Aggregate* **2021**, *2*, 1.